Hydrophone Spatial Averaging Correction for Acoustic Exposure Measurements From Arrays—Part I: Theory and Impact on Diagnostic Safety Indexes

Keith A. Wear [Senior Member, IEEE]

U.S. Food and Drug Administration, Silver Spring, MD 20993 USA.

Abstract

This article reports underestimation of mechanical index (MI) and nonscanned thermal index for bone near focus (TIB) due to hydrophone spatial averaging effects that occur during acoustic output measurements for clinical linear and phased arrays. TIB is the appropriate version of thermal index (TI) for fetal imaging after ten weeks from the last menstrual period according to the American Institute of Ultrasound in Medicine (AIUM). Spatial averaging is particularly troublesome for highly focused beams and nonlinear, nonscanned modes such as acoustic radiation force impulse (ARFI) and pulsed Doppler. MI and variants of TI (e.g., TIB), which are displayed in real-time during imaging, are often not corrected for hydrophone spatial averaging because a standardized method for doing so does not exist for linear and phased arrays. A novel analytic inverse-filter method to correct for spatial averaging for pressure waves from linear and phased arrays is derived in this article (Part I) and experimentally validated in a companion article (Part II). A simulation was developed to estimate potential spatial-averaging errors for typical clinical ultrasound imaging systems based on the theoretical inverse filter and specifications for 124 scanner/transducer combinations from the U.S. Food and Drug Administration (FDA) 510(k) database from 2015 to 2019. Specifications included center frequency, aperture size, acoustic output parameters, hydrophone geometrical sensitive element diameter, etc. Correction for hydrophone spatial averaging using the inverse filter suggests that maximally achievable values for MI, TIB, thermal dose (t_{43}), and spatial-peak-temporal-average intensity (I_{spta}) for typical clinical systems are potentially higher than uncorrected values by (means $\pm$ standard deviations) 9% $\pm$ 4% (ARFI MI), 19% $\pm$ 15% (ARFI TIB), 50% $\pm$ 41% (ARFI t_{43}), 43% $\pm$ 39% (ARFI I_{spta}), 7% $\pm$ 5% (pulsed Doppler MI), 15% $\pm$ 11% (pulsed Doppler TIB), 42% $\pm$ 31% (pulsed Doppler t_{43}), and 33% $\pm$ 27% (pulsed Doppler I_{spta}). These values correspond to frequencies of 3.2 $\pm$ 1.3 (ARFI) and 4.1 $\pm$ 1.4 MHz (pulsed Doppler), and the model predicts that they would increase with frequency. Inverse filtering for hydrophone spatial averaging significantly improves the accuracy of estimates of MI, TIB, t_{43}, and I_{spta} for ARFI and pulsed Doppler signals.

Index Terms—

Acoustic output measurement; exposimetry; hydrophone; spatial averaging

keith.wear@fda.hhs.gov.

I.   Introduction

A.   Acoustic Exposimetry

The goal of this work was to develop an inverse-filter method for prediction of, and correction for, underestimation of acoustic exposure safety parameters due to hydrophone spatial averaging effects that occur during acoustic output measurements for clinical linear and phased arrays. As discussed in a seminal 1988 special issue from this journal devoted to ultrasound metrology [1], acoustic pressure transmitted from medical ultrasound transducers is usually measured with hydrophones [2]–[4].

Acoustic pressure parameters include peak compressional pressure (p_c), peak rarefactional pressure (p_r), and pulse intensity integral (pii) (see [5, Eq. 5.4.3–1]). Two parameters that are used to characterize acoustic output of diagnostic ultrasound systems in the context of regulatory evaluation are directly proportional to pii: spatial-peak pulse average intensity (I_{sppa}) and spatial-peak temporal average intensity (I_{spta}) [6], [7].

Exposure safety parameters may be derived from pressure measurements. These include mechanical index (MI) and thermal index (TI), which are indicators of likelihoods of mechanical and thermal bioeffects, respectively. MI and TI are displayed in real-time on most clinical ultrasound imaging systems. Nonscanned pulses (e.g., acoustic radiation force impulse (ARFI), spectral Doppler), which are repeatedly directed to a single location in tissue, have more potential for thermal bioeffects than scanned pulses, which are swept in a plane to generate 2-D images.

As will be seen in Section III-C, the relative error (absolute error divided by the true value) in MI is often approximately equal to the relative error in p_r. The relative error in one version of TI, TIB (TI for bone near focus), is often approximately equal to the relative error in $(pii)^{1/2}$. According to the British Medical Ultrasound Society (BMUS) and the American Institute of Ultrasound in Medicine (AIUM), TIB is the appropriate version of TI for fetal imaging after ten weeks from the last menstrual period [8], [9]. BMUS also recommends TIB for neonatal general and cardiac imaging [8]. BMUS and AIUM have issued guidelines regarding maximum recommended combinations of TI and exposure time that are considered safe [8], [9].

B.   Hydrophone Measurements of Nonlinear Ultrasound

Medical ultrasound transducers often transmit pressure waves with sufficiently high amplitude to result in nonlinear propagation, especially during acoustic output measurements performed in water. Nonlinear spectra contain ample energy not just near the transducer fundamental (i.e., driving) frequency but also near harmonics (i.e., integer multiples) of the fundamental frequency. High-pressure amplitude results in improved signal-to-noise ratio (SNR) for many common diagnostic modes, including ARFI [10], harmonic imaging [11], M-mode, and pulsed Doppler [12].

However, nonlinearity creates added difficulty for hydrophone measurements for two reasons. First, because of the presence of harmonics, nonlinear signals have far broader bandwidths than linear signals. The sensitivity of a hydrophone may exhibit substantial

frequency dependence over the broad band of harmonic frequencies contained in the nonlinear pressure signal. Therefore, when converting hydrophone output voltage waveforms to acoustic pressure waveforms, a deconvolution of voltage with sensitivity should be performed instead of simply dividing voltage by a constant sensitivity factor (e.g., in units of V/MPa) [13]–[20].

Second, nonlinear signals have complicated beam shapes. The aggregate beam contains components at the fundamental frequency and multiple harmonic frequencies. The beam widths of the harmonic components decrease as harmonic frequency increases [21]–[25]. For sufficiently high harmonic frequencies (i.e., when harmonic component beamwidth becomes comparable to, or smaller than, the hydrophone sensitive element size), hydrophone measurements are compromised by spatial averaging artifacts. Therefore, spatial averaging acts like a low-pass filter.

C. Hydrophone Spatial Averaging Correction

Previous methods for correction for hydrophone spatial averaging effects have assumed sources with circular symmetry. A pioneering method, recognized by IEC 62127–1 [6], involves measurement of a frequency-independent scale factor to apply when linear pressure waves are incident on the hydrophone [26]. Spatial averaging for a circularly symmetric hydrophone may be concisely represented by a "running mean" integral [27]. Subsequent approaches are applicable to linear and nonlinear pressure waves. Most involve numerical computation of spatial averaging effects [28]–[32]. Another one involves an analytic inverse-filter spatial averaging correction that explicitly accounts for frequency-dependent hydrophone effective sensitive element size [25]. This method has been validated for nonlinear signals measured with: 1) needle hydrophones at diagnostic pressure levels [33]; 2) membrane hydrophones at diagnostic pressure levels [34]; and 3) needle and fiber-optic hydrophones at therapeutic pressure levels [35].

D. Outline of This Article

The goal of this article is to extend the analytic inverse-filter approach from sources with circular geometry to sources with linear or phased array geometry, the most common form for diagnostic ultrasound transducers. First, the theoretical analytic spatial averaging filter (SAF) is derived. Second, a simulation to predict underestimation of acoustic exposure safety parameters for clinical linear and phased arrays is presented. Third, the effect of underestimation of TIB on thermal dose t_{43} (sometimes called "thermally equivalent time") is analyzed. Fourth, results for predictions of underestimates of acoustic exposure safety parameters for clinical ARFI and pulsed Doppler signals are presented. Fifth, the results are discussed in the context of regulatory considerations, recommendations for safe use of medical ultrasound by professional organizations, and potential for bioeffects. Finally, concluding remarks are made.

II. Theory

A. Pressure Field at Focal Plane

The spectrum of the pressure field will be represented as having components at a fundamental frequency f_1 (the driving frequency of the source transducer) and at harmonic frequencies nf_1 (where n is an integer) due to nonlinear propagation. The nth harmonic component of the pressure field will be assumed to be separable into the product of axial and lateral factors [36]

$$P(nf_1, x, y) = s(nf_1)w_n(x, y) \tag{1}$$

where x and y are spatial coordinates in the hydrophone measurement plane, which is perpendicular to the propagation direction. The total pressure is the sum of $P(nf_1, x, y)$ over all harmonic components. The first factor, $s(nf_1)$, gives the relative strength of the nth harmonic on the beam propagation axis. When an inverse temporal Fourier transform is applied to the total pressure, the result is a sum of weighted, phase-shifted, complex sinusoids. For example, a model form is given in [25, Eq. (10)] (converting from cylindrical to rectangular coordinates)

$$p(t, x, y) = \sum_{n=1}^{N} s(nf_1)\exp\left[i\left(2\pi nf_1 t - \frac{\pi}{4}\right)\right]w_n(x, y) . \tag{2}$$

Equation (2) has previously been shown to be useful for modeling spatial averaging effects of axially symmetric tone bursts measured using axially symmetric hydrophones [25], [33].

The dependence of the pressure field of the nth harmonic on transverse coordinates x and y in the focal plane will be approximated as the product of two Gaussians

$$w_n(x, y) = w_{nx}(x)w_{ny}(y) \tag{3}$$

where

$$w_{nx}(x) = \exp(ig_{nx}x^2)\exp\left[-\frac{x^2}{2\sigma_{nx}^2}\right] \tag{4}$$

and

$$w_{ny}(y) = \exp(ig_{ny}y^2)\exp\left[-\frac{y^2}{2\sigma_{ny}^2}\right] . \tag{5}$$

Here, g_{nx} and g_{ny} determine the dependence of phase on transverse coordinates. Gaussian parameters σ_{nx} and σ_{ny} describe the widths of the Gaussian beam profiles in the lateral and elevational dimensions. Note that the full-width half-maxima (FWHM) in lateral and elevational dimensions are given by $\text{FWHM}_x = \sigma_{nx}2(2\ln2)^{1/2} \approx 2.35\sigma_{nx}$ and $\text{FWHM}_y = \sigma_{ny}2(2\ln2)^{1/2} \approx 2.35\sigma_{ny}$. For axially symmetric sources, $g_{nx} = g_{ny} = g_n$ and $\sigma_{nx} = \sigma_{ny} = \sigma_n$. There are many cases in which σ_n obeys an approximate power-law relationship with

harmonic number, $\sigma_n \approx \sigma_1/n^q$ [21]–[23], [25]. The value of q has been measured to be near 0.8 for diagnostic-pressure-level, axially symmetric fields [25].

The effects of spatial averaging may be found by integrating the free field (i.e., the field in the absence of a hydrophone) over the surface of an imaginary hydrophone sensitive element with an appropriate frequency-dependent "effective" sensitive element size [37]. The effective sensitive element size can differ substantially from the geometrical sensitive element size, especially at low frequencies [37]. The frequency-dependent effective sensitive element size may be inferred from directivity measurements [38]. Frequency-dependent effective sensitive element sizes have been measured and reported for membrane [37], [39]–[42], needle [41], [43], and fiber-optic [44] hydrophones.

The next task is to derive expressions for σ_{nx} and σ_{ny} in terms of transducer geometrical parameters. Then harmonic pressure fields will be integrated across the frequency-dependent effective hydrophone sensitive element surface in order to predict hydrophone output voltage.

A transducer source $A(x_s, y_s)$ with uniform surface pressure p_0 and rectangular aperture of dimensions L_x and L_y may be represented by

$$A(x_s, y_s) = p_0 \text{rect}\left(\frac{x_s}{L_x}\right)\text{rect}\left(\frac{y_s}{L_y}\right) \tag{6}$$

where x_s and y_s are coordinates in the source plane, and $\text{rect}(v) = 1$ for $|v| < 0.5$ and 0 otherwise. This simplification is valid for linear and phased arrays when the element pitch (distance between neighboring element centers) is much greater than the kerf (distance between neighboring element edges) and small enough so that grating lobes are well-separated from the main diffraction lobe [45]. In the focal plane, the pressure distribution for the fundamental component is shown in (7) at the bottom of the page, where z = focal distance, λ_1 = fundamental wavelength, $k_1 = 2\pi/\lambda_1$, and $\text{sinc}(v) = \sin(\pi v)/(\pi v)$ [46], [47]. This representation of the focal pattern of a linear or phased array is a simplification of a more general form for the far field (or focal plane) response that takes into account convolutions with individual element responses [45], [48]. As shown in Fig. 1, a sinc function can be approximated over its central lobe ($|v| < 1$) by a Gaussian function according to $\text{sinc}(v) \approx \exp(-2v^2)$, where $v = (L_x x)/(\lambda_1 z)$, with root-mean-squared error (RMSE) = 4.5%, so that

$$U(x, y) = \frac{i p_0}{\lambda_1 z}\exp(-ik_1 z)\exp\left[-i\frac{k_1}{2z}(x^2 + y^2)\right]L_x L_y \text{sinc}\left(\frac{L_x x}{\lambda_1 z}\right)\text{sinc}\left(\frac{L_y y}{\lambda_1 z}\right) \tag{7}$$

$$\text{sinc}\left(\frac{L_x x}{\lambda_1 z}\right) \approx \exp\left[-\frac{2L_x^2 x^2}{\lambda_1^2 z^2}\right] = \exp\left[-\frac{x^2}{2\sigma_{nx}^2}\right] \tag{8}$$

where

$$\sigma_{1x} = \frac{\lambda_1 z}{2L_x} . \tag{9}$$

The FWHM for the fundamental frequency component from a rectangular aperture is approximately given by $\text{FWHM}_{1x} \approx 1.2\lambda_1 z/L_x$ [47], which is consistent with the approximate expression given above, $\text{FWHM}_{1x} \approx 2.4\sigma_{nx}$.

The spatial averaging integral will be performed over the hydrophone sensitive element surface, which will be assumed here to be small enough to be confined to the central region where the sinc function pressure distribution is approximately a Gaussian function ($|v| < 1$, see Fig. 1). As suggested above, beamwidth parameters for harmonics may be given by $\sigma_{nx} = \sigma_{1x}/n^{qx}$ and $\sigma_{ny} = \sigma_{1y}/n^{qy}$. The exponents q_x and q_y, reported previously for circular sources for which $q = q_x = q_y$ [21]–[23], [25], will be measured for three clinical array sources in Part II [49].

B. Spatial Averaging Filter

Spatial averaging may be modeled by performing the integral of the normalized pressure field magnitude over the hydrophone frequency-dependent effective sensitive element surface [25]. The SAF $S_p(nf_1)$ is proportional to this integral divided by the hydrophone effective sensitive element surface area, $\pi a_{\text{eff}}^2(f)$ [25]. At the focal point, because of symmetries of the pressure field and the hydrophone, the integral may be performed over just one quadrant, with the result multiplied by 4, as shown in (10) at the bottom of the page, where $|w_n(x, y)|$ is the normalized acoustic pressure magnitude corresponding to the nth harmonic

$$S_p(nf_1) = \frac{4}{\pi a_{\text{eff}}^2(nf_1)} \int_0^{a_{\text{eff}}(nf_1)} dy \int_0^{\sqrt{a_{\text{eff}}^2(nf_1) - y^2}} dx |w_n(x, y)| \tag{10}$$

$$|w_n(x, y)| = \exp\left[-\frac{x^2}{2\sigma_{nx}^2}\right]\exp\left[-\frac{y^2}{2\sigma_{ny}^2}\right]. \tag{11}$$

Equation (10) ignores the effects of phase of the pressure field, which have been shown to be negligible for hydrophone SAFs in many common cases [25]. The integral over x can be simplified to reduce the formula to a 1-D integral for rapid computation, as shown in (12) at the bottom of the page, where erf( ) = the error function and the following definite integral has been used:

$$S_p(nf_1) = \frac{4}{\pi a_{\text{eff}}^2(nf_1)} \int_0^{a_{\text{eff}}(nf_1)} dy \exp\left[-\frac{y^2}{2\sigma_{ny}^2}\right]\frac{\sigma_{nx}\sqrt{\pi}}{\sqrt{2}}\text{erf}\left(\frac{\sqrt{a_{\text{eff}}^2(nf_1) - y^2}}{\sigma_{nx}\sqrt{2}}\right) \tag{12}$$

$$\int_0^\beta \exp(-\alpha x^2)dx = \frac{\sqrt{\pi}}{2\sqrt{\alpha}}\text{erf}(\beta\sqrt{\alpha}) = \frac{\sigma\sqrt{\pi}}{\sqrt{2}}\text{erf}\left(\frac{\beta}{\sigma\sqrt{2}}\right) \tag{13}$$

and the last equality assumes that $a = 1/(2\sigma^2)$.

A simpler formula for the SAF may be obtained by approximating the integral over the circular sensitive element with an integral over an equivalent square sensitive element as shown in Fig. 2. Using numerical integration, it can be shown that the overlap between the circular and square areas is 91%. Substituting the equivalent square hydrophone sensitive element for the circular hydrophone sensitive element trades some area near the periphery of the circle (9%) for slightly more distant area just within the corners of the square but outside the circle. Therefore, since the Gaussian pressure signal decreases monotonically with distance from the axis, the equivalent square hydrophone would be expected to yield SAF values slightly less than the circular hydrophone. In addition, the square shape might produce edge effects that would be more pronounced compared with the circular shape. Although a square region may seem like a simplistic approximation for a circular region, it should be recalled that, due to imperfections in the manufacturing process, sensitive elements for real hydrophones are not perfectly circular either, so even assuming a circular shape is an approximation. An analogous comparison can be made for circular and square source apertures [47].

Taking the frequency-dependent side length of the square to be $b_{\text{eff}}(f)$, the areas of the circular and square sensitive elements may be equated to give $b_{\text{eff}}^2(f) = \pi a_{\text{eff}}^2(f)$ or $b_{\text{eff}}(f) = \sqrt{\pi}a_{\text{eff}}(f)$. This gives (14), as shown at the bottom of the page.

In many practical cases, focusing will be much tighter along the long axis of the array than along the short axis so that spatial averaging in the elevation dimension may be ignored. This is equivalent to taking the limit of (14) as $\sigma_{ny} \to \infty$. For $\gamma \ll 1$, $\text{erf}(\gamma) = 2\gamma/\sqrt{\pi}$. Then the SAF becomes

$$
\begin{aligned}
S_{\text{p}}(nf_1) &\approx \frac{4}{\pi a_{\text{eff}}^2(nf_1)} \int_0^{b_{\text{eff}}(nf_1)/2} dy \int_0^{b_{\text{eff}}(nf_1)/2} dx |w_n(x,y)| \\
&\approx \frac{2\sigma_{nx}\sigma_{ny}}{a_{\text{eff}}^2(nf_1)} \text{erf}\left[\frac{\sqrt{\pi}a_{\text{eff}}(nf_1)/2}{\sigma_{nx}\sqrt{2}}\right] \text{erf}\left[\frac{\sqrt{\pi}a_{\text{eff}}(nf_1)/2}{\sigma_{ny}\sqrt{2}}\right]
\end{aligned}
\tag{14}
$$

$$
S_p(nf_1) \approx \frac{\sqrt{2}\sigma_{nx}}{a_{\text{eff}}(nf_1)} \text{erf}\left[\frac{\sqrt{\pi}a_{\text{eff}}(nf_1)/2}{\sigma_{nx}\sqrt{2}}\right].
\tag{15}
$$

As a check, $S_{\text{p}}(nf_1) \to 1$ as $\gamma \to 0$, as expected.

Fig. 3 shows lateral FWHM (circles) and elevational FWHM (asterisks) for ten harmonics from a 6-MHz array ($L_x = 50$ mm, $L_y = 8$ mm, $z = 75$ mm). Fig. 3 also shows frequency-dependent hydrophone effective sensitive element diameters $d_{\text{eff}}(f) = 2a_{\text{eff}}(f)$ (dashed lines) for five membrane hydrophones with d_g (hydrophone geometrical sensitive element diameter) = 200, 400, 600, 800, and 1000 μm [37]. At low frequencies, $d_{\text{eff}}(f) > d_g$ while at high frequencies, $d_{\text{eff}}(f)$ asymptotically approaches values close to d_g [37], [42] (dashed lines). Spatial averaging in this example is a concern in the lateral dimension because FWHM$_{\text{lateral}}$ (circles) is always on the order of, or smaller than, $d_{\text{eff}}(f)$ (dashed lines), even

for the smallest value for d_g (200 μm). However, spatial averaging is much less of a concern in the elevational dimension because $FWHM_{elev}$ (asterisks) $\gg$ $FWHM_{lateral}$ (circles).

Fig. 4 shows SAF, $S_p(nf_1)$, for the configuration in Fig. 3 and $d_g = 200$ μm. The equivalent square hydrophone approximation from (15) is a good approximation to the 2-D integral form in (10). Fig. 4 illustrates that $S_p(nf_1)$ is a low-pass filter.

In the companion article (Part II), experimental data for ARFI and pulsed Doppler waveforms will be used to validate this theory and the underlying assumptions: 1) approximation of arrays by rectangular sources; 2) approximation of harmonic beam radial dependences as Gaussian functions across hydrophone sensitive element surfaces; 3) neglecting phases of integrands; and 4) approximation of hydrophone sensitive element boundaries by squares.

III. Methods

A. Simulation of Waveforms

A simulation was conducted in order to predict the effects of hydrophone spatial averaging on MI and TIB for conditions under which typical commercial diagnostic ultrasound scanners operate.

The effects of hydrophone spatial averaging on a pulse may be simulated by taking a digitized, time-domain radio-frequency (RF) pulse, applying a fast Fourier transform (FFT), multiplying by the SAF, applying an inverse FFT, and then comparing values of p_c, p_r, and pii of filtered and unfiltered pulses.

In order to obtain clinically relevant hydrophone and pulse parameters, the Food and Drug Administration (FDA) medical device database was searched over all FDA-cleared diagnostic ultrasound imaging system premarket (510(k)) notifications between 2015 and 2019. The range of years was recent enough to ensure that information was still relevant to machines in current use but large enough to capture a wide variety of scanner/transducer combinations. Premarket notifications typically provide acoustic output measurement methodology, including hydrophone type and sensitive element size, and acoustic output reporting tables (AORTs) in formats specified in national [5] and international [50] standards. However, 510(k) notifications typically do not provide digitized time-domain RF pulses, which (as explained in the previous paragraph) are needed to quantitatively assess the effects of spatial averaging.

Therefore, a method was developed to reconstruct simulated time-domain RF pulses from acoustic output parameters provided in the AORTs. Pulses were characterized by four parameters: f_1, p_r, pulse duration (PD), and pii. The first two pulse parameters, f_1 and p_r, were directly specified in the AORTs, although p_r had to be corrected for derating. PD and pii were computed from data in the AORTs using well-known formulas. See, for example, [5, Eqs. 5.4.7–1 and 5.4.10–1]. PD is defined as 1.25 multiplied by the interval between the times when the time integral of the square of the instantaneous acoustic pressure reaches 10% and 90% of its final value [51].

The parametric model for simulated pulses was a variation of a form that has been shown to be accurate for modeling nonlinear medical ultrasound pulses [28], [52], [53]

$$p(t) = m(t) \left[\sum_{n=1}^{100} \frac{1}{n^s} \sin\left(2\pi f_1 t + \frac{\pi}{4}\right) \right]. \tag{16}$$

The envelope function, $m(t)$, had three phases: a rising portion proportional to $[1 - \exp(-t/t_1)]$ followed by a constant middle portion of duration t_m, followed by a decaying trailing portion proportional to $\exp(-t/t_2)$, where $t_1 = 1/(2 f_1)$ and $t_2 = 1/(4 f_1)$ [53]. The exponent s controlled the degree of nonlinearity. A low value of s (e.g., $s = 1$) corresponded to a highly nonlinear signal with high harmonic content while a high value of s (e.g., s 3) corresponded to a relatively linear signal with low harmonic content.

The values for f_1 and p_r in the simulated pulses were constrained to exactly match the values specified in the AORTs. A 2-D space was searched in order to find the parameter pair (t_m, s) for the simulated pulse that minimized the average mean square difference between simulated and AORT values for PD and pii. The accuracy of this pulse simulation method will be evaluated using experimentally acquired RF pulses in the companion article (Part II) [49].

The algorithm reconstructed a single pulse from all the data in each AORT. However, some data provided in the AORT were acquired at the depth of the maximum attenuated rarefactional pressure (z_{MI}) while other data were acquired at the depth of the maximum attenuated pulse intensity integral (z_{pii}). These two depths were usually quite close to each other but not necessarily equal. Therefore, data in AORTs were derived from two pulse waveforms instead of just one. In order to minimize errors due to separation between z_{MI} and z_{pii}, only AORT data sets for which z_{MI} and z_{pii} differed by less than 10% were used in the simulation.

In order to compute the SAF, an empirical form for frequency-dependent effective sensitive element diameter $d_{eff}(f) = 2a_{eff}(f)$ as a function of nominal geometrical sensitive element diameter d_g and frequency was used [37]. The exponent q_x that describes the dependence of lateral beamwidth on harmonic number ($\sigma_{nx} = \sigma_{1x}/n^{qx}$) was set to 0.77 (ARFI) and 0.76 (pulsed Doppler), based on averages of experimental measurements in Part II [49]. Spatial averaging in the elevational dimension could be neglected because the elevational beamwidth $FWHM_{elev}(nf_1)$ was usually greater than $d_{eff}(nf_1)$ for all relevant harmonics.

Inverse filtering by division in frequency domain can produce erratic results at frequencies for which the value of the filter is much less than one. In order to suppress potential inverse filtering artifacts, pulse spectra were low-pass filtered, which is a common step for deconvolving hydrophone signals for the effects of sensitivity [15], [17], [35], [54] or spatial-averaging [35]. The low-pass filter was a six-point Butterworth filter with a cutoff at twenty times the transducer center (driving) frequency.

After inverse filtering, time-domain RF signals were rarefactional filtered. Rarefactional filtering has been shown to be useful for processing sensitivity-deconvolved hydrophone

measurements [16]. A rarefactional filter is a boxcar convolution that is applied in time domain only to negative pressures in the waveform. Rarefactional filtering smooths out negative lobes in the waveform while preserving positive lobes. Application of the rarefactional low-pass filter only to negative lobes is reasonable for nonlinear medical ultrasound signals because negative lobes contain far less harmonic content than positive lobes [3], [55], as illustrated in Fig. 5. The width of the rarefactional filter was one-tenth of the period of the waveform.

The SAF depends on the depth-dependent active aperture width, $L_x(z)$. $L_x(z)$ can be as large as the physical array width $L_{x\,\max}$ but can be smaller because of dynamic aperture that is often used near the transducer (e.g., propagation distance $z < L_{x\,\max}$). The optimal value for lateral F-number, $F/\# = z/L_x(z)$, is application-specific and involves a tradeoff between resolution and depth of field [56]. $F/\# < 1$ is problematic even for sophisticated beamforming algorithms such as synthetic aperture sequential beamforming [57].

The true value of $L_x(z)$ at the point of reported acoustic output measurements was not always known because of the proprietary nature of clinical dynamic aperture algorithms, although it was of course known that $L_x(z) \quad L_{x\,\max}$. For the purpose of reconstructing pulses from reported acoustic output data, it was assumed, however, that $L_x(z)$ was dynamically adjusted near the transducer in order to ensure that $F/\#$ was always maintained above a minimum acceptable value $F/\#_{\min}$. Therefore, $z/L(z) = \max[z/L_{x\,\max}, F/\#_{\min}]$. Note that if setting $z/L(z)$ equal to $F/\#_{\min}$ ever underestimated $L(z)$, then the lateral focal spot size (which is proportional to $F/\#$) would be overestimated, meaning that the effects of spatial averaging would be underestimated and therefore the estimates of effects on MI and TIB would be underestimated.

For modeling ARFI pressure waves, $F/\#_{\min}$ was chosen to be equal to 1.5, which has been commonly used for ARFI applications in myocardium [58], liver [10], [59]–[62], muscle [63], [64], kidney [63], [65], [66], arteries [67]–[69], blood [70], and tissue-mimicking materials [71]–[73]. A lower value of $F/\#_{\min} = 1$ has been used for artery [74] and median nerve [75].

For modeling pulsed Doppler pressure waves, $F/\#_{\min}$ was chosen to be equal to 2, which is a commonly cited value for pulsed Doppler [76]–[78]. However, values as low as approximately 1 have been used for peripheral vascular pulsed Doppler applications [79]. $F/\#_{\min} = 2$ has also been shown to be effective for imaging applications [80].

B. Formulas for MI and TI

MI, TI, and other acoustic output parameters are often expressed in terms of quantities that are measured in water and then "derated" or "attenuated" to estimate values that would be achieved in tissue. For p_r and other pressure-based quantities

$$p_{r,\,.3}(z) = p_r(z)10^{(-0.05\alpha z f_{\mathrm{awf}})}. \tag{17}$$

For pii and other intensity-based quantities

$$\text{pii}_{.3}(z) = \text{pii}(z)10^{(-0.1\alpha z f_{\text{awf}})} \tag{18}$$

where z is depth, f_{awf} is the acoustic working frequency, and α is usually taken to be 0.3 dB/(cm·MHz) [81], which is a conservative estimate for most human· tissues.

The MI is given by

$$\text{MI} = \frac{p_{r,\,.3}(z_{\text{MI}})f_{\text{awf}}^{-1/2}}{C_{\text{MI}}} \tag{19}$$

where z_{MI} is the depth of maximum attenuated pulse-pressure-squared integral and $C_{\text{MI}} = 1$ MPa/MHz$^{1/2}$ [51], [82].

There are three variations of TI: TIS (TI for soft tissue), TIB (TI for bone near focus), and TIC (TI for cranial bone) [51], [81], [83]. TI values are derived from measurements of power, W, or spatial-peak-temporal-average intensity, I_{spta}, or, in some cases, combinations of both measurements. Although W may be measured from a hydrophone planar scan, it is usually measured with a radiation force balance [1] and is therefore usually unaffected by hydrophone spatial averaging. However, I_{spta} is usually measured with a hydrophone and is therefore usually affected by spatial averaging.

Versions of TI that depend on W but not I_{spta} include scanned TIS, nonscanned TIS for apertures <1 cm^2, and TIC.

TIS for apertures >1 cm^2 is based on depth-dependent, attenuated versions of W and I_{spta}, which are denoted by $W_{.3}$ and $I_{\text{spta.3}}$. Unfortunately, depth-dependent $I_{\text{spta.3}}$ is not provided in AORTs, which complicates the analysis of the effect of hydrophone spatial averaging for TIS for apertures >1 cm^2.

TIB is computed from the minimum of two functions

$$\text{TIB} = \min\left[\frac{\sqrt{W_{.3}I_{\text{spta.3}}}}{50\,\text{mW}\cdot\text{cm}^{-1}}, \frac{W_{.3}}{4.4\text{mW}}\right]. \tag{20}$$

$W_{.3}$ and $I_{\text{spta.3}}$ in (20) are evaluated at the depth z_b where their product is maximum [83]. For nonscanned modes, AORTs include TIB, W_0 (power before derating), and z_b. These enable computation of $W_{.3}$ and the second term ("TIB$_W$") in (20). AORTs often also include the equivalent beam diameter, d_{eq} at depth z_b. This enables computation of the first term ("TIB$_{WI}$") in (20) using $I_{\text{spta}.3} = 4W_{.3}/\left(\pi d_{\text{eq}}^2\right)$ [81]. By identifying the minimum of the two terms, it is therefore possible to ascertain which term determined the TIB in the AORT.

When TIB is determined by TIB$_{WI}$ (which is often for ARFI and pulsed Doppler pulses, as will be seen in Section IV-A), TIB is directly proportional to attenuated $(I_{\text{spta}})^{1/2}$ evaluated at the appropriate depth (z_b). Since I_{spta} is directly proportional to pii [51], TIB in these cases is directly proportional to $(\text{pii})^{1/2}$.

C. Relative Errors and Depths of Measurements

The measurement X_m of a parameter X (e.g., p_r, pii, MI, TI, TIB, or I_{spta} in attenuated or nonattenuated forms) may be expressed as the sum of its true value and measurement error X_e

$$X_m = X + X_e. \tag{21}$$

The relative error may be expressed by

$$\varepsilon_X = \frac{X_e}{X} = \frac{X_m - X}{X}. \tag{22}$$

It is useful to relate relative errors in the diagnostic exposure indexes (e.g., MI, TI, TIB, or I_{spta}) to relative errors in fundamental pressure parameters (e.g., p_r and pii). Note that application of a derating factor will not affect the relative error in (22) when the same factor is applied to both numerator and denominator. Ambiguity can arise, however, when the diagnostic exposure index is modeled at a different location in the beam diffraction pattern than where the pressure measurement is performed.

The theory in Section II models spatial averaging of pressure at the geometrical focus of a focusing transducer. However, MI may be measured at the point of maximum attenuated (derated) pulse-pressure-squared integral [51], which may be located closer to the transducer than the geometrical focus because of multiplication by the derating factor that decays with depth. This shift may be small in many common cases, including moderate-to-strongly focusing transducers. In these cases, it may be assumed that the relative errors in MI are approximately equal to relative errors in focal-plane p_r. This does not assume that p_r is equal at the two locations. It only assumes that the relative error in p_r is approximately equal at the two locations (because of similar beamwidths at the two locations).

TIB is measured at the depth z_b along the beam axis where the product of attenuated output power and attenuated I_{spta} is maximum [51]. This also may be located closer to the transducer than the geometrical focus. In fact, this shift is greater for TIB than MI because of the presence of two derating factors in the first term of (20). This shift may be small in many common cases, including moderate-to-strongly focusing transducers. In these cases, it may be assumed that relative errors in TIB are approximately equal to relative errors in the square root of focal-plane pii (see Section III-B). This does not assume that pii is equal at the two locations. It only assumes that the relative error in $(pii)^{1/2}$ is approximately equal at the two locations. There may be cases in which the locations of measurements of TIB are sufficiently far from the focal plane that the relative errors in $(pii)^{1/2}$ cannot be considered approximately equal at measurement and focal planes. These cases will be considered in Section V-B.

D. TI and Temperature Rise

TI is defined as the ratio of the attenuated acoustic power at the depth of interest to the power necessary to raise the tissue equilibrium temperature by 1 °C [83]. For example, a TI

value of 2 would imply a 2 °C increase in equilibrium temperature [83]. As has been discussed elsewhere [83], there are many sources of inaccuracy of TI as it is implemented in commercial diagnostic ultrasound systems. Nevertheless, the AIUM Technical Standards Committee, in the most recent comprehensive analysis of TI, declined to recommend major changes [83]. TI is attractive because of its simplicity, its utility in providing real-time feedback during clinical exams, and the lack of an obvious practical alternative.

BMUS and AIUM have issued tables of recommended maximum scanning times as functions of TI values (see Section V-B). These recommendations allow for the possibility that TIB can underestimate temperature rise ΔT by a factor of 2 at times [8], [9]. The relationship between TIB and ΔT can vary considerably on a case-by-case basis because of variations in many variables (e.g., anatomy, attenuation, perfusion, etc.) that are not accounted for in each individual calculation of TIB. In order to estimate typical errors in pulsed Doppler and ARFI thermal dose due to underestimation of TIB arising from hydrophone spatial averaging, the present analysis will assume that, after averaging over a variety of conditions, the average value of TI will be roughly comparable to the average value in ΔT. This approximation is based on a literature review given in Section V-E.

E. Impact of TI on Thermal Dose

It is instructive to investigate the effects of hydrophone spatial averaging on thermal dose, which is an indicator of potential for thermal bioeffects. Thermal dose for a pulse sequence, t_{43}, is a function of temperature rise and exposure duration. Thermal dose is sometimes called "thermally equivalent time" [84]. For a constant temperature T applied over a time t

$$t_{43} = t R^{(T - 43°C)/C_T} \tag{23}$$

where $R = 4$ for T 43 °C and $R = 2$ for $T > 43$ °C [9], [85]. $C_T = 1$ °C is included to make the exponent dimensionless [9]. The utility of t_{43} has been demonstrated in studies on animal tissue that establish the iso-effect tradeoff between temperature rise and exposure duration [86]. For humans, $T \approx 37$ °C $+ \Delta T$, where temperature rise, ΔT, is the increase in temperature beyond normal levels (and "normal" in this context corresponds to the absence of ultrasound or any external factor that could heat or cool tissue)

$$t_{43} = t R^{(\Delta T - 6°C)/C_T}. \tag{24}$$

The following discussion will derive a formula for the error in thermal dose estimate due to an error in the measurement of pii (e.g., due to hydrophone spatial averaging artifacts). A measurement of ΔT may be expressed as the sum of its true value and measurement error by

$$\Delta T_m = \Delta T + \Delta T_e. \tag{25}$$

TI is a relative index of ΔT [83]. The relative error in ΔT is

$$\varepsilon_{\Delta T} = \frac{\Delta T_e}{\Delta T} = \frac{\Delta T_m - \Delta T}{\Delta T}. \tag{26}$$

Then it follows that

$$\frac{\Delta T_{\mathrm{m}}}{\Delta T} = 1 + \varepsilon_{\Delta T} \tag{27}$$

$$\frac{\Delta T_{\mathrm{e}}}{\Delta T_{\mathrm{m}}} = \frac{\varepsilon_{\Delta T}}{1 + \varepsilon_{\Delta T}}. \tag{28}$$

From the discussion in Sections III-B and III-C, it follows that

$$\varepsilon_{\Delta T} = \sqrt{\varepsilon_{\mathrm{pii}}}. \tag{29}$$

The error in the exponent of (23) (e.g., due to hydrophone spatial averaging artifacts) is then

$$\frac{\Delta T_{\mathrm{e}}}{C_{\mathrm{T}}} = \frac{\Delta T_{\mathrm{m}}}{C_{\mathrm{T}}} \frac{\sqrt{\varepsilon_{\mathrm{pii}}}}{1 + \sqrt{\varepsilon_{\mathrm{pii}}}}. \tag{30}$$

The estimate of TIB based on hydrophone measurements without spatial averaging correction (provided in the AORT) may be used for T_{m}. With T_{m} obtained from the AORT and $\varepsilon_{\mathrm{pii}}$ obtained from simulation (see Section III-A), T_{e} may be found from (30) and the estimated relative error in thermal dose t_{43} is

$$\gamma = \frac{t_{43\,\mathrm{m}} - t_{43}}{t_{43}} = \frac{t\,R^{(\Delta T + \Delta T_{\mathrm{e}} - 6°)/C_{\mathrm{T}}} - t\,R^{(\Delta T - 6°)/C_{\mathrm{T}}}}{t\,R^{(\Delta T - 6°)/C_{\mathrm{T}}}}$$

$$= R^{\Delta T_e/C_T} - 1. \tag{31}$$

IV. Results

A. Hydrophone Types and Spatial Averaging Corrections

Out of 221 submissions involving linear, phased, and convex arrays in the FDA premarket notification database for 2015–2019, 141 provided unambiguous information regarding hydrophone type (membrane, needle, or capsule) and nominal geometrical sensitive element diameter. The most common hydrophone type was membrane, being used in 115 out of 141 submissions (82%). For the 141 submissions with unambiguous hydrophone information, spatial averaging corrections were explicitly applied in 49 submissions (35%), explicitly not applied in 72 submissions (51%), and not mentioned in 20 submissions (14%). When spatial averaging corrections were not mentioned, it seems likely that they were not applied, which would imply that in 92 out of 141 submissions (65%), spatial averaging corrections were not applied. Even when spatial averaging corrections were applied, the most common method was one that had been derived for transducers with circular symmetry producing linear pressure waves at the focal plane [26] and therefore inappropriate for arrays with rectangular geometry producing linear or nonlinear pressure waves at the focus. When spatial averaging corrections were not applied, the most common hydrophone geometrical sensitive element diameter was 400 μm.

Table I shows means and standard deviations of acoustic working frequencies and acoustic exposure indexes. Fig. 6 shows a scatter plot of the first and second terms ("TIB_{WI}" and "TIB_W") from the right side of (20) computed from AORT data for pulsed Doppler signals. TIB_{WI} was less than TIB_W in 100% of the ARFI (10/10) and pulsed Doppler (114/114) AORTs analyzed. Therefore, TIB in these cases was determined by TIB_{WI}. On some occasions, TIB_{WI} was less than the AORT-specified TIB, which is inconsistent with (20). This may be due to round-off errors in values in AORTs.

B. Simulation

Fig. 7 shows a simulated Doppler pulse reconstructed from data from an AORT from a premarket (510(k)) notification. For all data analyzed from premarket notifications cleared by FDA between 2015 and 2019, there were 114 Doppler pulses and 10 ARFI pulses with unambiguous hydrophone information and without spatial averaging correction. These pulses were used to analyze the effects of the inverse-filter spatial averaging correction on pulse pressure parameters (p_c, p_r, pii). For ARFI pulses, the RMSE for PD and pii values computed from simulated pulses versus values derived directly from data from the AORTs were 2.5% and 2.5%, respectively. For Doppler pulses, the RMSE values for PD and pii were 6.1% and 5.2%, respectively. These low values for RMSE suggest that the simulated pulses were accurate representations of the unknown pulses that produced the values in the AORTs. The accuracy of the pulse reconstruction method will be directly tested with experimentally acquired RF pulses in Part II [49].

Fig. 7 also shows an inverse-spatial-averaging-filtered pulse. The inverse-SAF was a high-pass filter that boosted harmonic components relative to the fundamental component, resulting in higher, sharper, compressional peaks. Fig. 8 shows simulated spectra before and after inverse-spatial-averaging filtering.

Fig. 9 shows predictions of percentage errors in p_c, p_r, pii, MI, and I_{spta} for simulated ARFI and Doppler pulses in the absence of spatial averaging correction, based on data from AORTs. The abscissa is the ratio of the hydrophone geometrical sensitive element diameter d_g to the product of the fundamental wavelength λ_1 and the F/# (ratio of focal length to array width). The product $\lambda_1 F$/# is an index of the fundamental focal spot width because $\text{FWHM}_{1x} \approx 1.2\lambda_1 F$/# (see Section II-A). There is substantial vertical spread in the Doppler p_c and pii, which means that there are other sources of variability besides ($d_g/\lambda_1 F$/#). Still, ($d_g/\lambda_1 F$/#) appears to be a useful parameter for analyzing trends.

Table II shows means, standard deviations, and ranges of percentage differences between corrected (for hydrophone spatial averaging) and uncorrected values of pressure parameters and exposure indexes. Based on (31), using the corrected value of TIB rather than the uncorrected value would imply an increase in the thermal dose (t_{43}) of 50% ± 41% (ARFI) and 42% ± 31% (pulsed Doppler).

V. Discussion

A. Hydrophone Spatial Averaging and Sensitivity Corrections

Early approaches for hydrophone spatial averaging correction were limited to circularly symmetric transducers and were either based on linear acoustics [26] or numerical instead of analytic methods [28]. In this article, an approximative, analytic, inverse-filter method for spatial averaging correction, originally developed for circularly symmetric transducers and linear/nonlinear beams [25], [33] has been extended to rectangularly symmetric arrays and linear/nonlinear beams. Rectangularly symmetric arrays are far more common in diagnostic applications than circularly symmetric transducers. In Part II, the method is validated with experimental data from 12 array/hydrophone combinations [49].

Until 2019, the FDA guidance for diagnostic ultrasound systems recommended conformance with the "Output Display Standard" (ODS) published jointly by AIUM and the National Electrical Manufacturers Association (NEMA) as valid methodology for evaluation of MI and TI [5]. (The 2019 revision of the FDA guidance relies on IEC 62359 [51] for this.) The ODS provided criteria (based on linear ultrasound beams) for maximum hydrophone diameter to maintain spatial averaging errors below a tolerable level. It subsequently stated that if these criteria could not be met, then "a geometrical hydrophone diameter (or greatest dimension) equal to or less than 0.6 mm shall be used." This statement reflected conventional wisdom and available hydrophone technology at the time the ODS was published (2004). Manufacturers using hydrophones with geometrical diameters less than or equal to 0.6 mm to evaluate MI and TI without spatial averaging corrections have been in conformance with the ODS and FDA guidance. Moreover, until now there has been no published method for correction for hydrophone spatial averaging from rectangularly symmetric arrays that manufacturers could have used, even if they had wanted to.

However, recently it has been demonstrated with circularly symmetric transducers that hydrophones with sensitive element geometrical diameters of 0.6 mm can produce significant spatial averaging artifacts at diagnostic-level pressures, with error magnitudes up to 70% in pii and I_{spta} (see [34, Figs. 11 and 12]). The companion article (Part II) demonstrates that similar errors are also possible for linear array source transducers for both ARFI and pulsed Doppler waveforms and hydrophones with sensitive element geometrical diameters of 0.6 mm [49].

I_{sppa} and I_{spta} are also used in the regulatory evaluation of diagnostic ultrasound imaging systems [6], [7]. I_{sppa} and I_{spta} were measured on early commercial diagnostic ultrasound imaging systems [87], [88], thus determining maximum recommended intensity levels for regulatory evaluation and providing a basis for claims of "substantial equivalence" regarding acoustic exposure safety for subsequent systems. Since I_{sppa} and I_{spta} are both directly proportional to pii, they are also impacted by hydrophone spatial averaging. The extent to which early measurements of I_{sppa} and I_{spta} were affected by spatial averaging is difficult to ascertain due to incomplete information currently available regarding waveforms and hydrophones involved in the measurements (but may be investigated in a future study). Therefore, uncertainty remains regarding what maximum values of I_{sppa} and I_{spta} would be appropriate if properly corrected for hydrophone spatial averaging.

Hydrophone spatial averaging compounds another phenomenon that can lead to underestimation of acoustic exposure parameters, which is acoustic saturation. Acoustic saturation results from excess absorption of harmonics of nonlinear waveforms measured in water. Acoustic saturation has been shown to be relevant at clinical levels of acoustic output and becomes increasingly important as frequency and focal length increase [89].

Membrane hydrophones tend to be preferred over needle and capsule hydrophones for diagnostic ultrasound transducer characterization because of their relatively broad bandwidth and uniform frequency response (sensitivity) [6]. More complicated (i.e., less uniform) frequency responses are found for needle [53], [90]–[92], capsule [15], and fiber-optic [16], [93]–[96] hydrophones. The nonuniform sensitivity of needle, capsule, and fiber-optic hydrophones can be counteracted by performing sensitivity deconvolution [13]–[20], [54], [97]. However, sensitivity deconvolutions were rarely encountered in the FDA 510(k) database from 2015 to 2019.

B. Mechanical Index (MI) and Thermal Index (TI)

Most diagnostic ultrasound scanners display MI and TI in real-time alongside the image to provide the operator with indications of potential for bioeffects. These indexes inform operators' adjustments of gain settings in order to obtain useful diagnostic images with exposure As Low As Reasonably Achievable (ALARA) [98]. Diagnostic ultrasound system manufacturers compute MI and TI based on acoustic pressure measurements performed in water tanks using hydrophones. These measurements are derated (attenuated) in order to account for the effects of tissue attenuation *in vivo* [5].

As discussed in Section III-E, thermal dose depends on a combination of temperature rise and exposure duration. TI (e.g., TIB) is an index of temperature rise. In order to guide clinical use of diagnostic ultrasound, professional societies have developed recommendations for maximum exposure duration as a function of TI. Current recommendations by the AIUM are shown in Table III and are thoroughly discussed elsewhere along with similar recommendations by other authorities [9]. The recommendations in Table III are based on empirical data that relate temperature rise, exposure duration, and bioeffects in animal studies [85], [99]–[101]. The degree of relevance of animal data to clinical potential for bioeffects is unknown.

There is a safety margin between recommended TI/exposure duration combinations in Table III and bioeffects thresholds. The safety margin is motivated by the finding that TI values can underestimate temperature elevations by a factor of up to two [8], [9], [102], [103]. This can happen, for instance, when the ultrasound beam passes through a fluid (e.g., urine or amniotic fluid) that attenuates much less than the value commonly used for derating, 0.3 dB/(cm·MHz). Simulation analysis suggests that, for reasons other than inaccurate derating, TI in unscanned modes often overestimates temperature elevation [104], [105]. The recommendations in Table III do not consider the effects of hydrophone spatial averaging. However, since thermal dose is directly proportional to exposure time, the effects of spatial averaging may be counteracted by reducing maximum recommended exposure times in Table III.

As stated in Section III-C, TIB is measured at the depth z_b along the beam axis where the product $W_{.3}I_{spta.3}$ is maximum [51]. This is likely to be located closer to the transducer than the geometrical focus (where the model from Section II predicts hydrophone spatial averaging). The separation between z_b and the geometrical focus may not be great for moderate-to-strongly focusing transducers but increases as $F/\#$ increases. Moving backward from the geometrical focus toward the transducer, beam widths increase and therefore the effects of hydrophone spatial averaging decrease. Therefore, for weakly focusing transducers, the effects of hydrophone spatial averaging would be expected to be less than that predicted by the model from Section II. In addition, if z_b for a weakly focusing transducer is determined from intensity measurements that are not corrected for spatial averaging, it will tend to be underestimated (i.e., pushed closer to the transducer) because the magnitude of underestimation of $I_{spta.3}$ increases with depth until the geometrical focus, implying that the depth of estimated maximum for $W_{.3}I_{spta.3}$ will be shifted toward the transducer. This can lead to inaccurate estimates for z_b that compromise the validity of the TIB measurement.

C. Alternatives to MI and TI

Due to shortcomings of MI and TI, alternative indexes have been proposed. An alternative formulation for MI that takes viscoelastic properties of tissue into account has been proposed for ARFI imaging [106]. An alternative formulation for TI, based on functional fits to temperature rises estimated by simulation over broad ranges of frequencies, apertures, and $F/\#$s, has been proposed for unscanned modes such as pulsed Doppler [105]. The "thermal dose index" (TDI) has been proposed to combine the effects of temperature rise and exposure duration [107].

These metrics likely have advantages over conventional MI and TI with regard for predicting likelihood of bioeffects. However, since their measured values are all based on fundamental acoustic output measurements of p_c, p_r, and pii, they will likely be subject to similar effects from hydrophone spatial averaging discussed in this article for MI and TIB. Therefore, they would be expected to benefit from improved data correction procedures (such as the one proposed in this article) that could be incorporated into standards such as IEC 62127-1 [6].

D. ARFI and Pulsed Doppler

Nonlinear pressure beams, such as those used in ARFI and pulsed Doppler applications, contain harmonic components at integer multiples of the transducer driving frequency. These nonlinear beams pose challenges for hydrophones because higher order harmonics can have beam widths on the order of, or even smaller than, the hydrophone sensitive element diameter. This leads to filtering out of high frequency content and subsequent underestimation of pii (from which TIB is computed). The degree of nonlinearity has less impact on MI than TIB because the rarefactional component of a nonlinear beam (from which MI is computed) has less harmonic content than the compressional component, as illustrated in Fig. 5. Therefore, as nonlinearity decreases, percentage errors in MI would not be expected to change much while percentage errors in TIB would be expected to diminish. These trends with respect to signal nonlinearity have been demonstrated with measurements and simulations for transducers with circular symmetry [34].

Shear wave elastography based on ARFI has been investigated for fetal applications including fetal brain [108], fetal lung [109], and maternal cervix [110], [111]. Shear wave elastography has been reported to have similar thermal effects as pulsed Doppler [112]. The effects of ARFI on fetal tissue have not been extensively characterized [112]. Fetal tissue is particularly vulnerable to thermal bioeffects [99]–[101], [113], [114]. Therefore, the results of this article give another reason for caution when considering ARFI for fetal applications.

Conditional increase in MI, beyond the maximum level recommended by FDA guidance (1.9) has been proposed in order to obtain deeper penetration and better SNR in sonographically challenging patients for ARFI-based shear wave velocity measurements [10], [115] and B-mode harmonic imaging (which also involves highly nonlinear beams) [11]. Conditional increase might extend useful diagnostic methods to a wider population with minimal increased risk of cavitation in nonfetal tissues without gas bodies [116]. Accounting for hydrophone spatial averaging is particularly important for applications when MI and/or TIB approach or exceed maximum recommended levels.

When considering conditional increase in MI, it is important to avoid combinations of frequency and peak rarefactional pressure that have been shown to produce cavitation in animal experiments. Empirical cavitation thresholds may be obtained from the literature describing experiments with circularly symmetric sources evaluated with membrane or needle hydrophones [117]–[122]. These thresholds have been tabulated based on their original literature values [116] and may be corrected for hydrophone spatial averaging from circular sources [34], as shown in Fig. 10. The maximum correction was 14%. However, the correction increases with frequency, and ARFI pulse sequences often use higher frequencies than 1.7 MHz, the highest frequency in Fig. 10. See Table I.

Temperature rise (ΔT) due to ARFI depends on many parameters including frequency, $F/\#$, frame rate, region of interest size, absorption coefficient, perfusion, and tissue thermal properties [123]. For example, for a 7.2 MHz, F/1.3 system (similar to F/1.5 systems considered here), imaging into a medium attenuating at 0.7 dB/(cm MHz) (porcine muscle), ΔT values on the order of 2 °C have·been measured with thermocouples, consistent with numerical models for configurations when effects of transducer heating may be ignored [124]. For clinical systems, transducer heating can also significantly contribute to ΔT, as has been demonstrated by simulation [58] and with infrared thermography in porcine muscle [125]. Simulation analysis suggests that ARFI can result in thermal dose values approaching recommended maximum dose thresholds if cooling interval between frames is too short [126].

Pulsed Doppler beams such as those used in spectral Doppler (as opposed to power Doppler or color flow imaging) are repeatedly directed at a specific target in the body [127] and are therefore associated with increased concern of thermal bioeffects than scanned modes (e.g., B-mode). Accordingly, pulsed Doppler beams from commercial diagnostic scanners in recent decades have been associated with higher values of I_{spta} (from which TIB is derived) than B-mode or color Doppler [128]. Fetal tissue is particularly vulnerable to thermal bioeffects [99]–[101], [113], [114]. Pulsed Doppler using clinical ultrasonic imaging systems has been associated with reversible liver damage [129] and impaired learning and

memory [130] in animal fetal studies. One study involving clinical transvaginal probes using pulsed Doppler and other modes on tissue-mimicking materials found that displayed TI consistently underestimated temperature rise measured using thermocouples [131]. Professional societies urge caution when using pulsed Doppler in pregnancy, particularly during the first trimester [132], [133]. The findings in this article that suggest that diagnostic scanners underestimate TIB for pulsed Doppler applications reinforce these recommendations.

E. Measurements of TIB and T for Pulsed Doppler Signals in Phantoms and Tissues

This section supports the approximation TIB $\approx$ T in Sections III-D and III-E.

One study, using 21 commercial scanner/transducer combinations (2.2–6.6 MHz in pulsed Doppler mode), found average TIB and average thermocouple-based T measurements to be within 10% of each other in a custom phantom [102]. Under "worst case" conditions (low attenuation due to propagation path including mostly fluid—e.g., urine or amniotic fluid), average TIB/ T was 0.6.

Another study, using a commercial scanner and 4 transducers (4 MHz in pulsed Doppler mode), found TIB to overestimate T in a phantom designed by the International Society of Ultrasound in Obstetrics and Gynecology (ISUOG), consisting of layers to simulate skin, other soft tissue, fluid, and bone [134]. While displayed values of TIB were approximately 3, thermocouple-based T measurements on the proximal surface of the bone mimic were only (mean $\pm$ standard deviation) 0.2 °C $\pm$ 0.1 °C (1 min exposure) to 0.7 °C $\pm$ 0.5 °C (30-min exposure).

Temperature rises in the ISUOG-phantom study tended to be lower than T estimates for tissues interrogated with pulsed Doppler beams at diagnostic $I_{spta.3}$ levels ($I_{spta.3} < 720$ mW/cm^2) [101]. A study of fetal sheep brain in utero (in which heating was enhanced due to proximity of the skull) reported thermocouple-based T measurements of 1.7 °C after 2-min exposure (3.5 MHz; I_{spta} not derated = 300 mW/cm^2) [135]. A study of unperfused human fetal vertebrae *in vitro* reported thermocouple-based T measurements of 0.6 ° C and 1.8 °C after 5-min exposure in samples of ages 14 and 39 weeks, respectively (3.5 MHz; I_{spta} not derated = 530 mW/cm^2) [136]. A computational model for pulsed Doppler exposure in the third trimester predicted T/TIB ratios ranging from 1.5 to 2.9 (TIB/ T: 0.34–0.67) for 2.25–3.5-MHz clinical array transducers [103], [137].

The ISUOG-phantom study was well-executed, coauthored by highly regarded ultrasound dosimetry experts, and provided valuable insights into potential thermal bioeffects in fetal ultrasound, especially regarding T at the transducer–skin interface. In addition, it was appropriate and commendable for these investigators to test a phantom design advocated by a major professional organization (ISUOG). However, the low values of T and T/TIB and the slow temperature rise times near the bone mimic (compared with measurements on tissues *in vitro* discussed in the previous paragraph) might be associated with suboptimal aspects of the ISUOG phantom design.

First, while the ISUOG-phantom skin mimic may have been realistic in approximating bulk attenuation in skin, its unrealistically low sound speed (1009 m/s) could have led to unrealistic sound-speed mismatches at skin-layer boundaries (1009 m/s versus 1541 m/s), resulting in excessive transmission losses (due to high impedance mismatches) and therefore unrealistically diminished ultrasound intensity propagating beyond the skin mimic to the bone mimic. (Computation of transmission coefficients would require knowledge of sound speeds and material densities, but the latter values were not provided [134]).

Second, although the ISUOG phantom geometry might simulate a typical anatomy, it might not capture the worst-case conditions with respect to thermal bioeffects in which the bone mimic would be aligned with the location of maximum value of $W_{.3}I_{\mathrm{spta.3}}$ for every transducer.

Third, the high-density polyethylene (HDPE) used to mimic bone in the ISUOG phantom is a homogeneous material that provides an attenuation coefficient, 4.5 dB/(cm·MHz), that is comparable to values found in cortical bone [138]. However, cancellous bone, which is especially abundant in vertebrae and calcaneus, has far higher levels of attenuation than cortical bone even though its mineral content and bone volume fraction are lower [138]. This apparent paradox is due to absorption mechanisms being different in cancellous and cortical bone. Computational models [139], [140] and experiments in phantoms [141] and bones [142] indicate that absorption in cancellous bone may be largely attributed to scattering (mode conversion) of longitudinal waves into shear waves by trabeculae followed by rapid absorption of scattered shear waves as they propagate away from trabeculae [143]. Attenuation coefficient has been reported to have an average value near 20 dB/(cm·MHz) in human cancellous femur [140]. Therefore, the HDPE bone mimic used in the ISUOG phantom might underestimate absorption and temperature rise in cancellous bone. Cancellous bone is well-developed in the later stages of gestation [144].

Much uncertainty remains regarding the relationship between pulsed Doppler TIB and T in human fetus *in vivo*. However, a relationship must be assumed in order to predict errors in thermal exposure predictions due to errors in TIB measurements (e.g., due to hydrophone spatial averaging). Based on available evidence, it does not seem excessively conservative to assume that $T \approx \mathrm{TIB}$.

F. Other Potential Bioeffects Within or Near Diagnostic Ultrasound Acoustic Output Levels

Investigations on bioeffects need to be accompanied by appropriate acoustic output characterization. Improved data correction procedures (such as the one proposed in this article) may improve the reliability and precision of such studies.

Bioeffects have been reported for certain circumstances with acoustic output within or near the diagnostic range, including increased fetal movement [145], neuromodulation [146], [147], nerve regeneration [148], impaired neuronal migration [149], angiogenesis [150], and bone fracture healing [116], [151].

Diagnostic ultrasound can produce streaming in fluids and has been used for differentiation of breast cysts from solid lesions [152]. Diagnostic ultrasound can produce capillary hemorrhage in tissues with gas bodies [153], [154].

Some studies have suggested a link between diagnostic ultrasound and incidence or severity of autism spectrum disorder [155], [156]. However, the AIUM Bioeffects Committee has reviewed these studies and has identified methodological flaws [157], [158]. A discussion of potential association of diagnostic ultrasound and autism may be found in [159].

Some bioeffects that are considered beneficial in some contexts (e.g., bone fracture healing, neuromodulation) could conceivably be associated with undesired effects in other contexts.

VI. Conclusion

Measurements of acoustic output from diagnostic ultrasound transducers can underestimate exposure parameters due to spatial averaging of focused beams across the hydrophone sensitive element. This is particularly problematic for beams that are either highly focused or nonlinear or both. On-screen exposure parameters, MI and TIB, are often not corrected for hydrophone spatial averaging effects partly because a standardized method for doing so does not exist for linear and phased arrays, the most common forms of diagnostic transducers. An analytic inverse-filter method for hydrophone spatial averaging correction has been derived in this article. It has been applied to data from clinical diagnostic ultrasound arrays operating at center frequencies of 3.2 ± 1.3 (ARFI) and 4.1 ± 1.4 MHz (pulsed Doppler). The inverse-filter analysis shows quantitatively how hydrophone spatial averaging errors increase with hydrophone sensitive element size, increase with frequency, and decrease with $F/\#$. In the companion article (Part II), the inverse-spatial-averaging-filter method is validated experimentally.

Acknowledgment

Biography

Keith A. Wear (Senior Member, IEEE) received the B.A. degree in applied physics from the University of California at San Diego, San Diego, CA, USA, and the M.S. and Ph.D. degrees in applied physics, with a Ph.D. minor in electrical engineering, from Stanford University, Stanford, CA.

He was a Postdoctoral Research Fellow with the Physics Department, Washington University, St. Louis, MO, USA. He is currently a Research Physicist with the U.S. Food and Drug Administration, Silver Spring, MD, USA.

Dr. Wear is a fellow of the Acoustical Society of America, the American Institute for Medical and Biological Engineering, and the American Institute of Ultrasound in Medicine (AIUM). He was the recipient of the 2019 AIUM Joseph H. Holmes Basic Science Pioneer Award. He is an Associate Editor-in-Chief of the IEEE Transactions on Ultrasonics, Ferroelectrics, and Frequency Control. He is an Associate Editor of three journals: IEEE Transactions on Ultrasonics, Ferroelectrics, and Frequency Control, the *Journal of the Acoustical Society of America, and Ultrasonic Imaging*. He was the Technical Program Chair of the 2008 IEEE International Ultrasonics Symposium, Beijing, China. He was the General Program Chair of the 2017 IEEE International Ultrasonics Symposium, Washington, DC, USA. He was elected to serve as the Vice-Chair from 2012 to 2014 and the Chair from 2014 to 2016 of the AIUM Technical Standards Committee. He was elected to serve as the Vice-Chair of the AIUM Bioeffects Committee from 2019 to 2021. He was elected to serve as the Secretary from 2010 to 2012, the Vice-Chair from 2012 to 2014, and the Chair from 2014 to 2016 of the AIUM Basic Science and Instrumentation Section, and the Secretary from 2010 to 2011, the Vice-Chair from 2011 to 2013, and the Chair from 2013 to 2015 of the AIUM Therapeutic Ultrasound Section. He is the Chair of the American Association of Physicists in Medicine Task Group 333 on Magnetic Resonance Guided Focused Ultrasound Quality Assurance.

References

[1]. Special Issue on Ultrasound Exposimetry, IEEE Trans. Ultrason., Ferroelectr., Freq. Control, vol. 35, no. 2, pp. 87–269, 3. 1988.

[2]. Harris GR, "Hydrophone measurements in diagnostic ultrasound fields," IEEE Trans. Ultrason., Ferroelectr., Freq. Control, vol. 35, no. 2, pp. 87–101, 3. 1988. [PubMed: 18290135]

[3]. Harris GR, "Progress in medical ultrasound exposimetry," IEEE Trans. Ultrason., Ferroelectr., Freq. Control, vol. 52, no. 5, pp. 717–736, 5 2005. [PubMed: 16048175]

[4]. Szabo TL, "Ultrasonic exposimetry and acoustic measurements," in Diagnostic Ultrasound Imaging: Inside Out, 2nd ed. San Diego, CA, USA: Academic, 2014, pp. 565–604.

[5]. Acoustic Output Measurement Standard for Diagnostic Ultrasound Equipment, Rev. 1, Arlington, VI, USA, NEMA, 2004.

[6]. Ultrasonics—Hydrophones—Part 1: Measurement and Characterization of Medical Ultrasonic Fields Up to 40 MHz, Standard IEC 62127–1, 2013.

[7]. (2019). Marketing Clearance of Diagnostic Ultrasound Systems and Transducers, Guidance for Industry and Food and Drug Administration Staff. [Online]. Available: https://www.fda.gov/media/71100/download

[8]. BMUS, "Guidelines for the safe use of diagnostic ultrasound equipment," Ultrasound, vol. 18, pp. 52–59, 12. 2010.

[9]. Harris GR et al., "Comparison of thermal safety practice guidelines for diagnostic ultrasound exposures," Ultrasound Med. Biol, vol. 42, no. 2, pp. 345–357, 2. 2016. [PubMed: 26626492]

[10]. Deng Y, Palmeri ML, Rouze NC, Rosenzweig SJ, Abdelmalek MF, and Nightingale KR, "Analyzing the impact of increasing mechanical index and energy deposition on shear wave speed reconstruction in human liver," Ultrasound Med. Biol, vol. 41, no. 7, pp. 1948–1957, 7. 2015. [PubMed: 25896024]

[11]. Deng Y, Palmeri ML, Rouze NC, Trahey GE, Haystead CM, and Nightingale KR, "Quantifying image quality improvement using elevated acoustic output in B-Mode harmonic imaging," Ultrasound Med. Biol, vol. 43, no. 10, pp. 2416–2425, 10. 2017. [PubMed: 28755792]

[12]. Bacon DR and Carstensen EL, "Increased heating by diagnostic ultrasound due to nonlinear propagation," J. Acoust. Soc. Amer, vol. 88, no. 1, pp. 26–34, 7. 1990. [PubMed: 2199548]

[13]. Wilkens V and Koch C, "Amplitude and phase calibration of hydrophones up to 70 MHz using broadband pulse excitation and an optical reference hydrophone," J. Acoust. Soc. Amer, vol. 115, no. 6, pp. 2892–2903, 6. 2004.

[14]. Hurrell A, "Voltage to pressure conversion: Are you gettingphased'by the problem?" Metrol. Ultrasound Med, vol. 1, no. 1, pp. 57–62, 2004.

[15]. Wear KA, Gammell PM, Maruvada S, Liu Y, and Harris GR, "Improved measurement of acoustic output using complex deconvolution of hydrophone sensitivity," IEEE Trans. Ultrason., Ferroelectr., Freq. Control, vol. 61, no. 1, pp. 62–75, 1. 2014. [PubMed: 24402896]

[16]. Wear K, Liu Y, Gammell P, Maruvada S, and Harris G, "Correction for frequency-dependent hydrophone response to nonlinear pressure waves using complex deconvolution and rarefactional filtering: Application with fiber optic hydrophones," IEEE Trans. Ultrason., Ferroelectr., Freq. Control, vol. 62, no. 1, pp. 152–164, 1. 2015. [PubMed: 25585399]

[17]. Eichstädt S, Wilkens V, Dienstfrey A, Hale P, Hughes B, and Jarvis C, "On challenges in the uncertainty evaluation for time-dependent measurements," Metrologia, vol. 53, no. 4, pp. S125–S135, 8. 2016.

[18]. Eichstädt S and Wilkens V, "GUM2DFT—A software tool for uncertainty evaluation of transient signals in the frequency domain," Meas. Sci. Technol, vol. 27, no. 5, 5 2016, Art. no. 055001.

[19]. Hurrell AM and Rajagopal S, "The practicalities of obtaining and using hydrophone calibration data to derive pressure waveforms," IEEE Trans. Ultrason., Ferroelectr., Freq. Control, vol. 64, no. 1, pp. 126–140, 1. 2017. [PubMed: 27479961]

[20]. Martin E and Treeby B, "Investigation of the repeatability and reproducibility of hydrophone measurements of medical ultrasound fields," J. Acoust. Soc. Amer, vol. 145, no. 3, pp. 1270–1282, 3. 2019. [PubMed: 31067926]

[21]. Du G and Breazeale MA, "Harmonic distortion of a finite amplitude Gaussian beam in a fluid," J. Acoust. Soc. Amer, vol. 80, no. 1, pp. 212–216, 7. 1986.

[22]. Reilly CR and Parker KJ, "Finite-amplitude effects on ultrasound beam patterns in attenuating media," J. Acoust. Soc. Amer, vol. 86, no. 6, pp. 2339–2348, 12. 1989. [PubMed: 2600313]

[23]. Ward B, Baker AC, and Humphrey VF, "Nonlinear propagation applied to the improvement of resolution in diagnostic medical ultrasound," J. Acoust. Soc. Amer, vol. 101, no. 1, pp. 143–154, 1. 1997. [PubMed: 9000731]

[24]. Hamilton MF, "Sound beams," in Nonlinear Acoustics, Hamilton MF, and Blackstock DT, Eds. San Diego, CA, USA: Academic, 1998, pp. 233–262.

[25]. Wear KA, "Considerations for choosing sensitive element size for needle and fiber-optic hydrophones—Part I: Spatiotemporal transfer function and graphical guide," IEEE Trans. Ultrason., Ferroelectr., Freq. Control, vol. 66, no. 2, pp. 318–339, 2. 2019. [PubMed: 30530326]

[26]. Preston RC, Bacon DR, and Smith RA, "Calibration of medical ultrasonic equipment-procedures and accuracy assessment," IEEE Trans. Ultrason., Ferroelectr., Freq. Control, vol. 35, no. 2, pp. 110–121, 3. 1988. [PubMed: 18290137]

[27]. Lum P, Greenstein M, Grossman C, and Szabo TL, "High-frequency membrane hydrophone," IEEE Trans. Ultrason., Ferroelectr., Freq. Control, vol. 43, no. 4, pp. 536–544, 7. 1996.

[28]. Zeqiri B and Bond AD, "The influence of waveform distortion on hydrophone spatial-averaging corrections—Theory and measurement," J. Acoust. Soc. Amer, vol. 92, no. 4, pp. 1809–1821, 10. 1992.

[29]. Radulescu EG, Lewin PA, Goldstein A, and Nowicki A, "Hydrophone spatial averaging corrections from 1 to 40 MHz," IEEE Trans. Ultrason., Ferroelectr., Freq. Control, vol. 48, no. 6, pp. 1575–1580, 11. 2001. [PubMed: 11800120]

[30]. Radulescu EG, Lewin PA, and Nowicki A, "1–60 MHz measurements in focused acoustic fields using spatial averaging corrections," Ultrasonics, vol. 40, nos. 1–8, pp. 497–501, 5 2002. [PubMed: 12159990]

[31]. Cooling MP, Humphrey VF, and Wilkens V, "Hydrophone area-averaging correction factors in nonlinearly generated ultrasonic beams," J. Phys., Conf. Ser, vol. 279, no. 1, pp. 1–6, 2011.

[32]. Bessonova O and Wilkens V, "Investigation of spatial averaging effect of membrane hydrophones for working frequencies in the low MHz range," in Proc. DAGA, 2012, pp. 937–938.

[33]. Wear KA and Liu Y, "Considerations for choosing sensitive element size for needle and fiber-optic hydrophones—Part II: Experimental validation of spatial averaging model," IEEE Trans. Ultrason., Ferroelectr., Freq. Control, vol. 66, no. 2, pp. 340–347, 2. 2019. [PubMed: 30530327]

[34]. Wear KA, Shah A, and Baker C, "Correction for hydrophone spatial averaging artifacts for circular sources," IEEE Trans. Ultrason., Ferroelectr., Freq. Control, vol. 67, no. 12, pp. 2674–2691, 12. 2020. [PubMed: 32746206]

[35]. Wear KA and Howard SM, "Correction for spatial averaging artifacts in hydrophone measurements of high-intensity therapeutic ultrasound: An inverse filter approach," IEEE Trans. Ultrason., Ferroelectr., Freq. Control, vol. 66, no. 9, pp. 1453–1464, 9. 2019. [PubMed: 31247548]

[36]. Soneson JE and Myers MR, "Gaussian representation of high-intensity focused ultrasound beams," J. Acoust. Soc. Amer, vol. 122, no. 5, pp. 2526–2531, 11. 2007. [PubMed: 18189543]

[37]. Wear KA, Baker C, and Miloro P, "Directivity and frequency-dependent effective sensitive element size of membrane hydrophones: Theory versus experiment," IEEE Trans. Ultrason., Ferroelectr., Freq. Control, vol. 66, no. 11, pp. 1723–1730, 11. 2019. [PubMed: 31352340]

[38]. Ultrasonics—Hydrophones—Part 3: Properties of Hydrophones for Ultrasonic Fields up to 40 MHz, document IEC 62127–3, 2013.

[39]. Shombert DG, Smith SW, and Harris GR, "Angular response of miniature ultrasonic hydrophones," Med. Phys, vol. 9, no. 4, pp. 484–492, 7. 1982. [PubMed: 7110078]

[40]. Harris GD and Shombert DG, "A pulsed near-field technique for measuring the directional characteristics of acoustic receivers," IEEE Trans. Sonics Ultrason, vol. SU-32, no. 6, pp. 802–808, 11. 1985.

[41]. Radulescu EG, Lewin PA, Nowicki A, and Berger WA, "Hydrophones' effective diameter measurements as a quasi-continuous function of frequency," Ultrasonics, vol. 41, no. 8, pp. 635–641, 11. 2003. [PubMed: 14585475]

[42]. Wilkens V and Molkenstruck W, "Broadband PVDF membrane hydrophone for comparisons of hydrophone calibration methods up to 140 MHz," IEEE Trans. Ultrason., Ferroelectr., Freq. Control, vol. 54, no. 9, pp. 1784–1791, 9. 2007. [PubMed: 17941384]

[43]. Wear KA, Baker C, and Miloro P, "Directivity and frequency-dependent effective sensitive element size of needle hydrophones: Predictions from four theoretical forms compared with measurements," IEEE Trans. Ultrason., Ferroelectr., Freq. Control, vol. 65, no. 10, pp. 1781–1788, 10. 2018. [PubMed: 30010557]

[44]. Wear KA and Howard SM, "Directivity and frequency-dependent effective sensitive element size of a reflectance-based fiber-optic hydrophone: Predictions from theoretical models compared with measurements," IEEE Trans. Ultrason., Ferroelectr., Freq. Control, vol. 65, no. 12, pp. 2343–2348, 12. 2018. [PubMed: 30281445]

[45]. Shung KK and Zippuro M, "Ultrasonic transducers and arrays," IEEE Eng. Med. Biol. Mag, vol. 15, no. 6, pp. 20–30, 12. 1996.

[46]. Goodman JW, Introduction to Fourier Optics. San Francisco, CA, USA: McGraw-Hill, 1968.

[47]. Szabo TL, "Beamforming," in Diagnostic Ultrasound Imaging—Inside OutSecond. Oxford, U.K.: Elsevier, 2014.

[48]. Macovski A, "Ultrasonic imaging using arrays," Proc. IEEE, vol. 67, no. 4, pp. 484–495, 4. 1979.

[49]. Wear KA, Shah A, Ivory AM, and Baker C, "Hydrophone spatial averaging correction for acoustic exposure measurements from arrays—Part II: Validation for ARFI and pulsed Doppler waveforms," IEEE Trans. Ultrason., Ferroelectr., Freq. Control, early access, Nov. 16, 2020, doi: 10.1109/TUFFC.2020.3037999.

[50]. Medical electrical Equipment—Part 2–37: Particular Requirements for the Basic Safety and Essential Performance of Ultrasonic Medical Diagnostic and Monitoring Equipment, document IEC 60601-2-37, Geneva, Switzerland: International Electrotechnical Commission, 2015.

[51]. Ultrasonics—Field Characterization—Test Methods for the Determination of Thermal and Mechanical Indices Related to Medical Diagnostic Ultrasonic Fields, document IEC 62359, 2017.

[52]. Ayme EJ and Carstensen EL, "Cavitation induced by asymmetric distorted pulses of ultrasound: Theoretical predictions," IEEE Trans. Ultrason., Ferroelectr., Freq. Control, vol. 36, no. 1, pp. 32–40, 1. 1989. [PubMed: 18284947]

[53]. Wear KA, Liu Y, and Harris GR, "Pressure pulse distortion by needle and fiber-optic hydrophones due to nonuniform sensitivity," IEEE Trans. Ultrason., Ferroelectr., Freq. Control, vol. 65, no. 2, pp. 137–148, 2. 2018. [PubMed: 29389648]

[54]. Eichstädt S and Wilkens V, "Evaluation of uncertainty for regularized deconvolution: A case study in hydrophone measurements," J. Acoust. Soc. Amer, vol. 141, no. 6, pp. 4155–4167, 6. 2017. [PubMed: 28618819]

[55]. Harris GR, "Are current hydrophone low frequency response standards acceptable for measuring mechanical/cavitation indices?" Ultrasonics, vol. 34, no. 6, pp. 649–654, 8. 1996. [PubMed: 8844965]

[56]. von Ramm OT and Smith SW, "Beam steering with linear arrays," IEEE Trans. Biomed. Eng, vol. 30, no. 8, pp. 438–452, 8. 1983. [PubMed: 6629379]

[57]. Kortbek J, Jensen JA, and Gammelmark KL, "Sequential beamforming for synthetic aperture imaging," Ultrasonics, vol. 53, no. 1, pp. 1–16, 1. 2013. [PubMed: 22809678]

[58]. Bouchard R, Dahl J, Hsu S, Palmeri M, and Trahey G, "Image quality, tissue heating, and frame rate trade-offs in acoustic radiation force impulse imaging," IEEE Trans. Ultrason., Ferroelectr., Freq. Control, vol. 56, no. 1, pp. 63–76, 1. 2009. [PubMed: 19213633]

[59]. Muller M, Gennisson JL, Deffieux T, Tanter M, and Fink M, "Quantitative viscoelasticity mapping of human liver using supersonic shear imaging: Preliminary *in vivo* feasibility study," Ultrasound Med Biol, vol. 35, no. 2, pp. 219–229, 2. 2009. [PubMed: 19081665]

[60]. Deffieux T, Montaldo G, Tanter M, and Fink M, "Shear wave spectroscopy for *in vivo* quantification of human soft tissues viscoelasticity," IEEE Trans. Med. Imag, vol. 28, no. 3, pp. 313–322, 3. 2009.

[61]. Bavu E et al., "Noninvasive *in vivo* liver fibrosis evaluation using supersonic shear imaging: A clinical study on 113 hepatitis C virus patients," Ultrasound Med. Biol, vol. 37, no. 9, pp. 1361–1373, 9. 2011. [PubMed: 21775051]

[62]. Deng Y, Rouze NC, Palmeri ML, and Nightingale KR, "Ultrasonic shear wave elasticity imaging sequencing and data processing using a verasonics research scanner," IEEE Trans. Ultrason., Ferroelectr., Freq. Control, vol. 64, no. 1, pp. 164–176, 1. 2017. [PubMed: 28092508]

[63]. Scola MR, Baggesen LM, and Gallippi CM, "Multi-push (MP) acoustic radiation force (ARF) ultrasound for assessing tissue viscoelasticity, *in vivo*," in Proc. 34th Annu. Int. Conf. IEEE Eng. Med. Biol. Soc, San Diego, CA, USA, 8. 2012, pp. 2323–2326.

[64]. Selzo MR, Moore CJ, Hossain MM, Palmeri ML, and Gallippi CM, "On the Quantitative Potential of Viscoelastic Response (VisR) Ultrasound Using the One-Dimensional Mass-Spring-Damper Model," IEEE Trans. Ultrason., Ferroelectr., Freq. Control, vol. 63, no. 9, pp. 1276–1287, 9. 2016. [PubMed: 27046848]

[65]. Hossain MM et al., "Evaluating renal transplant status using viscoelastic response (VisR) ultrasound," Ultrasound Med. Biol, vol. 44, no. 8, pp. 1573–1584, 8. 2018. [PubMed: 29754702]

[66]. Hossain MM et al., "Mechanical anisotropy assessment in kidney cortex using ARFI peak displacement: Preclinical validation and pilot *in vivo* clinical results in kidney allografts," IEEE Trans. Ultrason., Ferroelectr., Freq. Control, vol. 66, no. 3, pp. 551–562, 3. 2019. [PubMed: 30106723]

[67]. Dumont D, Behler RH, Nichols TC, Merricks EP, and Gallippi CM, "ARFI imaging for noninvasive material characterization of atherosclerosis," Ultrasound Med. Biol, vol. 32, no. 11, pp. 1703–1711, 11. 2006. [PubMed: 17112956]

[68]. Behler RH et al., "Acoustic radiation force beam sequence performance for detection and material characterization of atherosclerotic plaques: Preclinical, *ex vivo* results," IEEE Trans. Ultra- son., Ferroelectr., Freq. Control, vol. 60, no. 12, pp. 2471–2487, 12. 2013.

[69]. Czernuszewicz TJ and Gallippi CM, "On the feasibility of quantifying fibrous cap thickness with acoustic radiation force impulse (ARFI) ultrasound," IEEE Trans. Ultrason., Ferroelectr., Freq. Control, vol. 63, no. 9, pp. 1262–1275, 9. 2016. [PubMed: 26955026]

[70]. Scola MR et al., "ARFI ultrasound monitoring of hemorrhage and hemostasis *in vivo* in canine von Willebrand disease and hemophilia," Ultrasound Med. Biol, vol. 37, no. 12, pp. 2126–2132, 12. 2011. [PubMed: 22033127]

[71]. Selzo MR and Gallippi CM, "Viscoelastic response (VisR) imaging for assessment of viscoelasticity in Voigt materials," IEEE Trans. Ultrason., Ferroelectr., Freq. Control, vol. 60, no. 12, pp. 2488–2500, 12. 2013. [PubMed: 24297015]

[72]. Chen S, Fatemi M, and Greenleaf JF, "Quantifying elasticity and viscosity from measurement of shear wave speed dispersion," J. Acoust. Soc. Amer, vol. 115, no. 6, pp. 2781–2785, 6. 2004. [PubMed: 15237800]

[73]. Kijanka P and Urban MW, "Two-point frequency shift method for shear wave attenuation measurement," IEEE Trans. Ultrason., Ferroelectr., Freq. Control, vol. 67, no. 3, pp. 483–496, 3. 2020. [PubMed: 31603777]

[74]. Widman E, Maksuti E, Amador C, Urban MW, Caidahl K, and Larsson M, "Shear wave elastography quantifies stiffness in ex vivo porcine artery with stiffened arterial region," Ultrasound Med. Biol, vol. 42, no. 10, pp. 2423–2435, 10. 2016. [PubMed: 27425151]

[75]. Knight AE, Lipman SL, Ketsiri T, Hobson-Webb LD, and Nightingale KR, "On the challenges associated with obtaining reproducible measurements using SWEI in the median nerve," Ultrasound Med. Biol, vol. 46, no. 5, pp. 1092–1104, 5 2020. [PubMed: 32057471]

[76]. Christopher DA, Burns PN, Armstrong J, and Foster FS, "A high-frequency continuous-wave Doppler ultrasound system for the detection of blood flow in the microcirculation," Ultrasound Med. Biol, vol. 22, no. 9, pp. 1191–1203, 1996. [PubMed: 9123644]

[77]. Yu AC, Steinman AH, and Cobbold RS, "Transit-time broadening in pulsed Doppler ultrasound: A generalized amplitude modulation model," IEEE Trans. Ultrason., Ferroelectr., Freq. Control, vol. 53, no. 3, pp. 530–541, 3. 2006. [PubMed: 16555761]

[78]. Gran F, Udesen J, Nielsen MB, and Jensen JA, "Coded ultrasound for blood flow estimation using subband processing," IEEE Trans. Ultrason., Ferroelectr., Freq. Control, vol. 55, no. 10, pp. 2211–2220, 10. 2008. [PubMed: 18986869]

[79]. Jensen JA, "Spectral velocity estimation in ultrasound using sparse data sets," J. Acoust. Soc. Amer, vol. 120, no. 1, pp. 211–220, 7. 2006. [PubMed: 16875219]

[80]. Li Y and Zagzebski JA, "A frequency domain model for generating B-mode images with array transducers," IEEE Trans. Ultrason., Ferroelectr., Freq. Control, vol. 46, no. 3, pp. 690–699, 5 1999. [PubMed: 18238469]

[81]. Abbott JG, "Rationale and derivation of MI and TI–A review," Ultrasound Med Biol, vol. 25, no. 3, pp. 431–441, 3. 1999. [PubMed: 10374986]

[82]. Apfel RE and Holland CK, "Gauging the likelihood of cavitation from short-pulse, low-duty cycle diagnostic ultrasound," Ultrasound Med. Biol, vol. 17, no. 2, pp. 179–185, 1. 1991. [PubMed: 2053214]

[83]. Bigelow TA et al., "The thermal index: Its strengths, weaknesses, and proposed improvements," J. Ultrasound Med, vol. 30, no. 5, pp. 714–734, 5 2011. [PubMed: 21527623]

[84]. Models for Evaluation of Thermal Hazard in Medical Diagnostic Ultrasonic Fields, document IEC/TR 62799 2013.

[85]. O'Brien WD et al., "The risk of exposure to diagnostic ultrasound in postnatal subjects: Thermal effects," J. Ultrasound Med, vol. 27, no. 4, pp. 51735–51740, 4. 2008.

[86]. Sapareto SA and Dewey WC, "Thermal dose determination in cancer therapy," Int. J. Radiat. Oncol. Biol. Phys, vol. 10, no. 6, pp. 787–800, 4. 1984. [PubMed: 6547421]

[87]. Carson PL, Fischella PR, and Oughton TV, "Ultrasonic power and intensities produced by diagnostic ultrasound equipment," Ultrasound Med. Biol, vol. 3, no. 4, pp. 341–350, 1978. [PubMed: 653878]

[88]. Nyborg WL, "Biological effects of ultrasound: Development of safety guidelines. Part I: Personal histories," Ultrasound Med. Biol, vol. 26, no. 6, pp. 911–964, 7. 2000. [PubMed: 10996695]

[89]. Duck FA, "Acoustic saturation and output regulation," Ultrasound Med. Biol, vol. 25, no. 6, pp. 1009–1018, 7. 1999. [PubMed: 10461731]

[90]. Harris GR and Gammell PM, "Sensitivity measurements of piezo-electric polymer hydrophones from 0.2–2 MHz using a broadband-pulse technique," J. Acoust. Soc. Amer, vol. 105, no. 2, pp. 725–731, 2. 1999.

[91]. Fay B, Ludwig G, Lankjaer C, and Lewin PA, "Frequency response of PVDF needle-type hydrophones," Ultrasound Med. Biol, vol. 20, no. 4, pp. 361–366, 1. 1994. [PubMed: 8085292]

[92]. Zanelli CI and Howard SM, "A robust hydrophone for HIFU metrology," Therapeutic Ultrasound, vol. 829, p. 618, 12. 2006.

[93]. Morris P, Hurrell A, Shaw A, Zhang E, and Beard P, "A Fabry–Pérot fiber-optic ultrasonic hydrophone for the simultaneous measurement of temperature and acoustic pressure," J. Acoust. Soc. Amer, vol. 125, no. 6, pp. 3611–3622, 6. 2009. [PubMed: 19507943]

[94]. Krücker JF, Eisenberg A, Krix M, Lötsch R, Pessel M, and Trier H-G, "Rigid piston approximation for computing the transfer function and angular response of a fiber-optic hydrophone," J. Acoust. Soc. Amer, vol. 107, no. 4, pp. 1994–2003, 4. 2000. [PubMed: 10790026]

[95]. Howard SM, "Calibration of reflectance-based fiber-optic hydrophones," in Proc. IEEE Int. Ultrason. Symp. (IUS), 9. 2016, pp. 1–4.

[96]. Staudenraus J and Eisenmenger W, "Fibre-optic probe hydrophone for ultrasonic and shock-wave measurements in water," Ultrasonics, vol. 31, no. 4, pp. 267–273, 7. 1993.

[97]. Liu Y, Wear KA, and Harris GR, "Variation of high-intensity therapeutic ultrasound (HITU) pressure field characterization: Effects of hydrophone choice, nonlinearity, spatial averaging and complex deconvolution," Ultrasound Med. Biol, vol. 43, no. 10, pp. 2329–2342, 10. 2017. [PubMed: 28735734]

[98]. Bioeffects and Safety of Diagnostic Ultrasound, AIUM, Laurel, MD, USA, 1993.

[99]. Miller MW and Ziskin MC, "Biological consequences of hyperthermia," Ultrasound Med. Biol, vol. 15, no. 8, pp. 707–722, 1989. [PubMed: 2694557]

[100]. Miller MW, Nyborg WL, Dewey WC, Edwards MJ, Abramowicz JS, and Brayman AA, "Hyperthermic teratogenicity, thermal dose and diagnostic ultrasound during pregnancy: Implications of new standards on tissue heating," Int. J. Hyperthermia, vol. 18, no. 5, pp. 361–384, Sep-Oct. 2002. [PubMed: 12227925]

[101]. Abramowicz JS, Barnett SB, Duck FA, Edmonds PD, Hynynen KH, and Ziskin MC, "Fetal thermal effects of diagnostic ultrasound," J. Ultrasound Med, vol. 27, no. 4, pp. 541–560, 4. 2008. [PubMed: 18359908]

[102]. Shaw A, Pay NM, and Preston RC, "Assessment of the likely thermal index values for pulsed Doppler ultrasonic equipment–stages II and III: Experimental assessment of scanner/transducercombinations," National Physical Laboratory Report CMAM, vol. 12, 1998. [Online]. Available: https://eprintspublications.npl.co.uk/849/

[103]. Jago JR, Henderson J, Whittingham TA, and Mitchell G, "A comparison of AIUM/NEMA thermal indices with calculated temperature rises for a simple third-trimester pregnancy tissue model. American institute of ultrasound in medicine/national electrical manufacturers association," Ultrasound Med. Biol, vol. 25, no. 4, pp. 623–628, 5 1999. [PubMed: 10386738]

[104]. O'Brien WD and Ellis DS, "Evaluation of the unscanned soft-tissue thermal index," IEEE Trans. Ultrason., Ferroelectr., Freq. Control, vol. 46, no. 6, pp. 1459–1476, 11. 1999. [PubMed: 18244343]

[105]. O'Brien WD, Yang Y, and Simpson DG, "Evaluation of unscanned-mode soft-tissue thermal index for rectangular sources and proposed new indices," Ultrasound Med. Biol, vol. 30, no. 7, pp. 965–972, 7. 2004. [PubMed: 15313328]

[106]. Church CC, Labuda C, and Nightingale K, "Should the mechanical index be revised for ARFI imaging?" in Proc. IEEE Int. Ultrason. Symp, 10. 2012, pp. 17–20.

[107]. Ziskin MC, "The thermal dose index," J. Ultrasound Med, vol. 29, no. 10, pp. 1475–1479, 10. 2010. [PubMed: 20876902]

[108]. Diguisto C et al., "Ultrasonic elastography exploration of the foetal brain: A case of atypical choroid plexus papilloma," J. Obstetrics Gynaecol, vol. 37, no. 4, pp. 525–527, 5 2017.

[109]. Mottet N et al., "Feasibility of 2-D ultrasound shear wave elastography of fetal lungs in case of threatened preterm labour: A study protocol," BMJ Open, vol. 7, no. 12, 12. 2017, Art. no. e018130.

[110]. Carlson LC, Feltovich H, Palmeri ML, Dahl JJ, del Rio AM, and Hall TJ, "Estimation of shear wave speed in the human uterine cervix," Ultrasound Obstet Gynecol, vol. 43, no. 4, pp. 452–458, 4. 2014. [PubMed: 23836486]

[111]. Fruscalzo A, Mazza E, Feltovich H, and Schmitz R, "Cervical elastography during pregnancy: A critical review of current approaches with a focus on controversies and limitations," J. Med. Ultrason, vol. 43, no. 4, pp. 493–504, 10. 2016.

[112]. Issaoui M et al., "Shear wave elastography safety in fetus: A quantitative health risk assessment," Diagnostic Interventional Imag, vol. 99, no. 9, pp. 519–524, 9. 2018.

[113]. Church CC and Miller MW, "Quantification of risk from fetal exposure to diagnostic ultrasound," Prog. Biophys. Mol. Biol, vol. 93, nos. 1–3, pp. 331–353, Jan-Apr. 2007.

[114]. Salvesen KA, Lees C, Abramowicz J, Brezinka C, Haar GT, and Marsal K, "Safe use of Doppler ultrasound during the 11 to 13 6-week scan: Is it possible?" Ultrasound Obstet Gynecol, vol. 37, no.+6, pp. 625–628, 6. 2011. [PubMed: 21618312]

[115]. Deng Y, Palmeri ML, Rouze NC, Haystead CM, and Nightingale KR, "Evaluating the benefit of elevated acoustic output in harmonic motion estimation in ultrasonic shear wave elasticity imaging," Ultrasound Med. Biol, vol. 44, no. 2, pp. 303–310, 2. 2018. [PubMed: 29169880]

[116]. Nightingale KR et al., "Conditionally increased acoustic pressures in nonfetal diagnostic ultrasound examinations without contrast agents: A preliminary assessment," J. Ultrasound Med, vol. 34, no. 7, pp. 1–41, 7. 2015.

[117]. Hynynen K, "The threshold for thermally significant cavitation in dog's thigh muscle in vivo," Ultrasound Med. Biol, vol. 17, no. 2, pp. 69–157, 1991.

[118]. Frizzell LA, Chen E, and Lee C, "Effects of pulsed ultrasound on the mouse neonate: Hind limb paralysis and lung hemorrhage," Ultrasound Med. Biol, vol. 20, no. 1, pp. 53–63, 1. 1994. [PubMed: 8197627]

[119]. Hwang JH, Brayman AA, Reidy MA, Matula TJ, Kimmey MB, and Crum LA, "Vascular effects induced by combined 1-MHz ultrasound and microbubble contrast agent treatments *in vivo*," Ultrasound Med. Biol, vol. 31, no. 4, pp. 553–564, 4. 2005. [PubMed: 15831334]

[120]. Hwang JH, Tu J, Brayman AA, Matula TJ, and Crum LA, "Correlation between inertial cavitation dose and endothelial cell damage *in vivo*," Ultrasound Med. Biol, vol. 32, no. 10, pp. 1611–1619, 10. 2006. [PubMed: 17045882]

[121]. Miller DL, Dou C, and Lucchesi BR, "Are ECG premature complexes induced by ultrasonic cavitation electrophysiological responses to irreversible cardiomyocyte injury?" Ultrasound Med. Biol, vol. 37, no. 2, pp. 312–320, 2. 2011. [PubMed: 21257092]

[122]. Gateau J, Aubry JF, Pernot M, Fink M, and Tanter M, "Combined passive detection and ultrafast active imaging of cavitation events induced by short pulses of high-intensity ultrasound," IEEE Trans. Ultrason., Ferroelectr., Freq. Control, vol. 58, no. 3, pp. 517–532, 3. 2011. [PubMed: 21429844]

[123]. Palmeri ML and Nightingale KR, "On the thermal effects associated with radiation force imaging of soft tissue," IEEE Trans. Ultrason., Ferroelectr., Freq. Control, vol. 51, no. 5, pp. 551–565, 5 2004. [PubMed: 15217233]

[124]. Palmeri ML, Frinkley KD, and Nightingale KR, "Experimental studies of the thermal effects associated with radiation force imaging of soft tissue," Ultrasound Imag, vol. 26, no. 2, pp. 100–114, 4. 2004.

[125]. Issaoui M et al., "Temperature rise caused by shear wave elastography, pulse Doppler and B-mode in biological tissue: An infrared thermo-graphic approach," Ultrasound Med. Biol, vol. 46, no. 2, pp. 325–335, 2. 2020. [PubMed: 31735465]

[126]. Liu Y, Herman BA, Soneson JE, and Harris GR, "Thermal safety simulations of transient temperature rise during acoustic radiation force-based ultrasound elastography," Ultrasound Med. Biol, vol. 40, no. 5, pp. 1001–1014, 5 2014. [PubMed: 24548651]

[127]. Szabo TL, "Doppler modes," in Diagnostic Ultrasound Imaging: Inside Out, 2nd ed. San Diego, CA, USA: Academic, 2014, pp. 431–500.

[128]. Martin K, "The acoustic safety of new ultrasound technologies," Ultrasound, vol. 18, no. 3, pp. 110–118, 8. 2010.

[129]. Pellicer B, Herraiz S, Taboas E, Felipo V, Simon C, and Pellicer A, "Ultrasound bioeffects in rats: Quantification of cellular damage in the fetal liver after pulsed Doppler imaging," Ultrasound Obstet Gynecol, vol. 37, no. 6, pp. 643–648, 6. 2011. [PubMed: 20878673]

[130]. Schneider-Kolsky ME, Ayobi Z, Lombardo P, Brown D, Kedang B, and Gibbs ME, "Ultrasound exposure of the foetal chick brain: Effects on learning and memory," Int. J. Develop. Neurosci, vol. 27, no. 7, pp. 677–683, 11. 2009.

[131]. Miloro P, Martin E, and Shaw A, "Temperature elevation measured in a tissue-mimicking phantom for transvaginal ultrasound at clinical settings," Ultrasound, vol. 25, no. 1, pp. 6–15, 2. 2017. [PubMed: 28228820]

[132]. WFUMB/ISUOG, "WFUMB/ISUOG statement on the safe use of Doppler ultrasound during 11–14 week scans (or earlier) in pregnancy," Ultrasound Med. Biol, vol. 39, no. 3, p. 373, 2013. [PubMed: 23398714]

[133]. Statement on the Safe Use of Doppler Ultrasound During 11–14 Week Scans or Earlier in Pregnancy, AIUM, Laurel, MD, USA, 2016.

[134]. Smith SF, Miloro P, Axell R, ter Haar G, and Lees C, "*In vitro* characterisation of ultrasound-induced heating effects in the mother and fetus: A clinical perspective," Ultrasound, vol. 15, 9. 2020, Art. no. 1742271X2095319.

[135]. Duggan PM, Liggins GC, and Barnett SB, "Ultrasonic heating of the brain of the fetal sheep in utero," Ultrasound Med. Biol, vol. 21, no. 4, pp. 553–560, 1995. [PubMed: 7571148]

[136]. Doody C, Porter H, Duck FA, and Humphrey VF, "*In vitro* heating of human fetal vertebra by pulsed diagnostic ultrasound," Ultrasound Med. Biol, vol. 25, no. 8, pp. 1289–1294, 10. 1999. [PubMed: 10576271]

[137]. Whittingham TA, "Estimated fetal cerebral ultrasound exposures from clinical examinations," Ultrasound Med. Biol, vol. 27, no. 7, pp. 877–882, 7. 2001. [PubMed: 11476918]

[138]. Langton CM, Ali AV, Riggs CM, Evans GP, and Bonfield W, "A contact method for the assessment of ultrasonic velocity and broadband attenuation in cortical and cancellous bone," Clin. Phys. Physiol. Meas, vol. 11, no. 3, pp. 243–249, 8. 1990. [PubMed: 2245589]

[139]. Bossy E, Padilla F, Peyrin F, and Laugier P, "Three-dimensional simulation of ultrasound propagation through trabecular bone structures measured by synchrotron microtomography," Phys. Med. Biol, vol. 50, no. 23, pp. 5545–5556, 12 7 2005. [PubMed: 16306651]

[140]. Bossy E, Laugier P, Peyrin F, and Padilla F, "Attenuation in trabecular bone: A comparison between numerical simulation and experimental results in human femur," J. Acoust. Soc. Amer, vol. 122, no. 4, pp. 2469–2475, 10. 2007. [PubMed: 17902882]

[141]. Wear KA, "Mechanisms for attenuation in cancellous-bone-mimicking phantoms," IEEE Trans. Ultrason., Ferroelectr., Freq. Control, vol. 55, no. 11, pp. 2418–2425, 11. 2008. [PubMed: 19049921]

[142]. Pakula M, Padilla F, and Laugier P, "Influence of the filling fluid on frequency-dependent velocity and attenuation in cancellous bones between 0.35 and 2.5 MHz," J. Acoust. Soc. Amer, vol. 126, no. 6, pp. 3301–3310, 12. 2009. [PubMed: 20000944]

[143]. Wear KA, "Mechanisms of interaction of ultrasound with cancellous bone: A review," IEEE Trans. Ultrason., Ferroelectr., Freq. Control, vol. 67, no. 3, pp. 454–482, 3. 2020. [PubMed: 31634127]

[144]. Mulder L, Koolstra JH, de Jonge HW, and van Eijden TM, "Architecture and mineralization of developing cortical and trabecular bone of the mandible," Anatomy Embryol, vol. 211, no. 1, pp. 8–71, 1. 2006.

[145]. Fatemi M, Ogburn PL, and Greenleaf JF, "Fetal stimulation by pulsed diagnostic ultrasound," J. Ultrasound Med, vol. 20, no. 8, pp. 883–889, 8. 2001. [PubMed: 11503925]

[146]. Blackmore J, Shrivastava S, Sallet J, Butler CR, and Cleveland RO, "Ultrasound neuromodulation: A review of results, mechanisms and safety," Ultrasound Med. Biol, vol. 45, no. 7, pp. 1509–1536, 7. 2019. [PubMed: 31109842]

[147]. Tufail Y et al., "Transcranial pulsed ultrasound stimulates intact brain circuits," Neuron, vol. 66, no. 5, pp. 681–694, 6. 2010. [PubMed: 20547127]

[148]. Crisci AR and Ferreira AL, "Low-intensity pulsed ultrasound accelerates the regeneration of the sciatic nerve after neurotomy in rats," Ultrasound Med. Biol, vol. 28, no. 10, pp. 1335–1341, 10. 2002. [PubMed: 12467860]

[149]. Ang ES, Gluncic V, Duque A, Schafer ME, and Rakic P, "Prenatal exposure to ultrasound waves impacts neuronal migration in mice," Proc. Nat. Acad. Sci. USA, vol. 103, no. 34, pp. 12903–12910, 8. 22 2006. [PubMed: 16901978]

[150]. Barzelai S et al., "Low-intensity ultrasound induces angiogenesis in rat hind-limb ischemia," Ultrasound Med. Biol, vol. 32, no. 1, pp. 139–145, 1. 2006. [PubMed: 16364805]

[151]. Phillips RA, Stratmeyer ME, and Harris GR, "Safety and U.S. regulatory considerations in the nonclinical use of medical ultrasound devices," Ultrasound Med. Biol, vol. 36, no. 8, pp. 1224–1228, 8. 2010. [PubMed: 20447750]

[152]. Nightingale KR, Kornguth PJ, Walker WF, McDermott BA, and Trahey GE, "A novel ultrasonic technique for differentiating cysts from solid lesions: Preliminary results in the breast," Ultrasound Med. Biol, vol. 21, no. 6, pp. 745–751, 1995. [PubMed: 8571462]

[153]. Miller DL, Dong Z, Dou C, Patterson B, and Raghavendran K, "Pulmonary capillary hemorrhage induced by acoustic radiation force impulse shear wave elastography in ventilated rats," J. Ultrasound Med, vol. 38, no. 10, pp. 2575–2587, 10. 2019. [PubMed: 30702763]

[154]. Miller DL, "Mechanisms for induction of pulmonary capillary hemorrhage by diagnostic ultrasound: Review and consideration of acoustical radiation surface pressure," Ultrasound Med. Biol, vol. 42, no. 12, pp. 2743–2757, 12. 2016. [PubMed: 27649878]

[155]. Webb SJ, Garrison MM, Bernier R, McClintic AM, King BH, and Mourad PD, "Severity of ASD symptoms and their correlation with the presence of copy number variations and exposure to first trimester ultrasound," Autism Res, vol. 10, no. 3, pp. 472–484, 3. 2017. [PubMed: 27582229]

[156]. Rosman NP et al., "Association of prenatal ultrasonography and autism spectrum disorder," JAMA Pediatr, vol. 172, no. 4, pp. 336–344, 4. 2018. [PubMed: 29435580]

[157]. AIUM. (May 15, 2016). AIUM Responds to Autism Study. [Online]. Available: https://www.aium.org/soundWaves/article.aspx?aId=965&iId=20160907

[158]. AIUM, "Bioeffects literature reviews," J. Ultrasound Med, vol. 38, pp. 2525–2530, 2019. [PubMed: 31418897]

[159]. Abramowicz JS, "Ultrasound and autism: Association, link, or coincidence?" J. Ultrasound Med, vol. 31, no. 8, pp. 1261–1269, 8. 2012. [PubMed: 22837291]
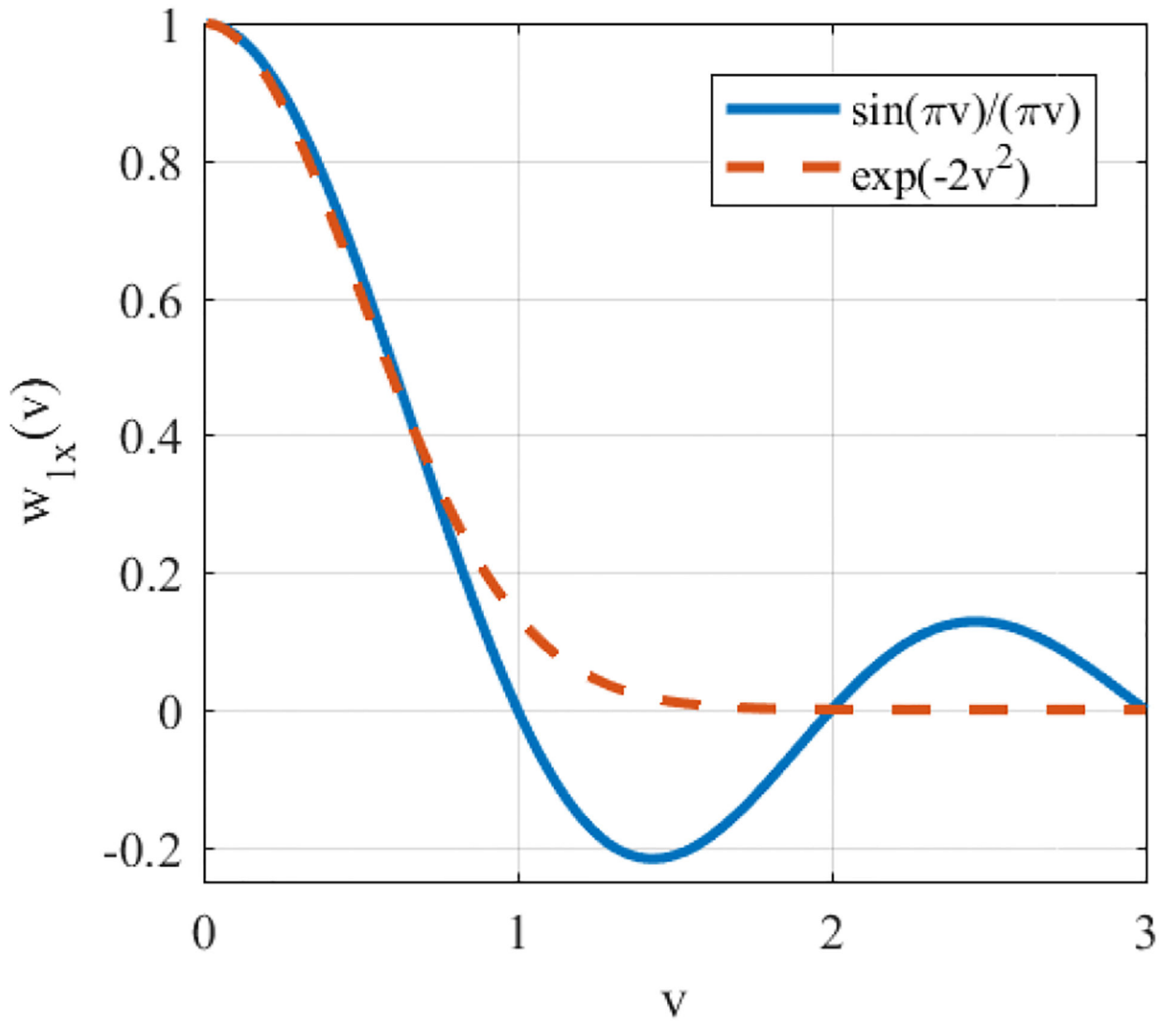
Author Manuscript

Author Manuscript

Author Manuscript

Author Manuscript

Fig. 1.
Gaussian approximation to $\mathrm{sinc}(v) = \sin(\pi v)/(\pi v)$ focal diffraction pattern in one dimension, where $v = (L_x x)/(\lambda_1 z)$.
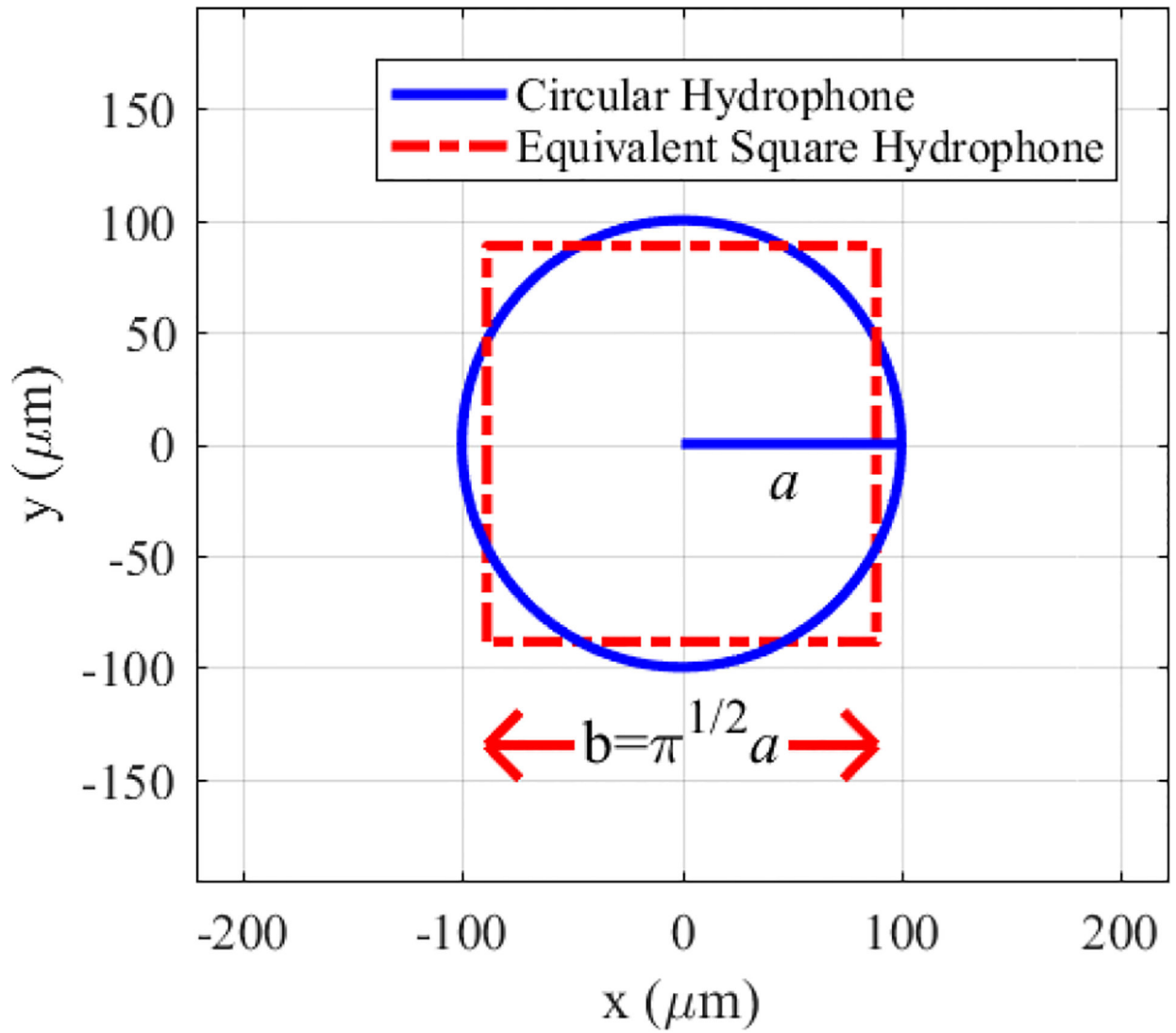
Fig. 2.
Circular hydrophone sensitive element and equivalent square hydrophone sensitive element.
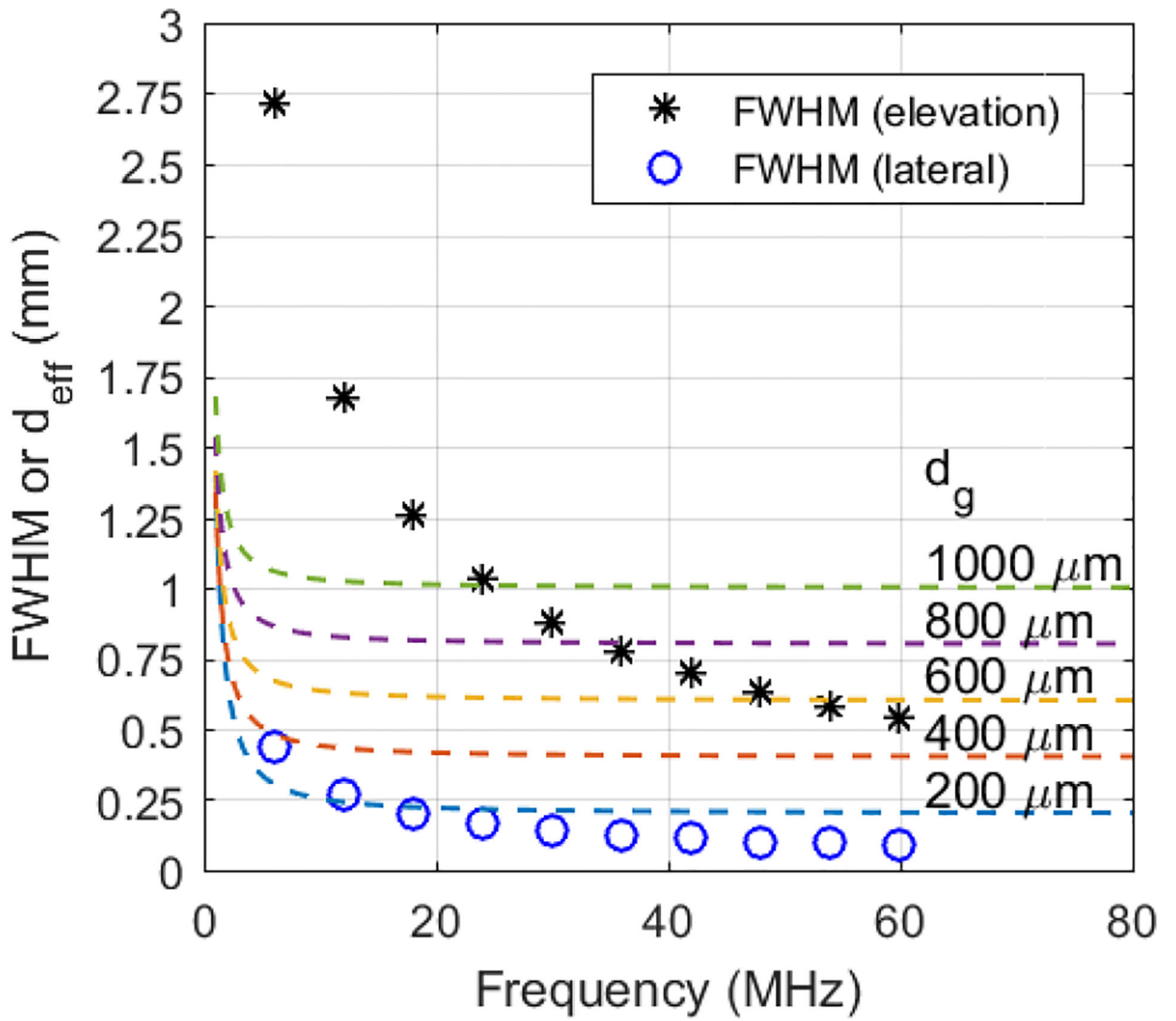
Fig. 3.
Lateral FWHM (circles) and elevational FWHM (asterisks) for ten harmonics. The transducer is a 6-MHz array that is 50 mm wide in the lateral dimension, 8 mm high in the elevation direction, and focused at 75 mm. Also shown are frequency-dependent hydrophone effective sensitive diameters d_{eff} (dashed lines) for five membrane hydrophones with geometrical diameters d_{g}: 200, 400, 600, 800, and 1000 μm.
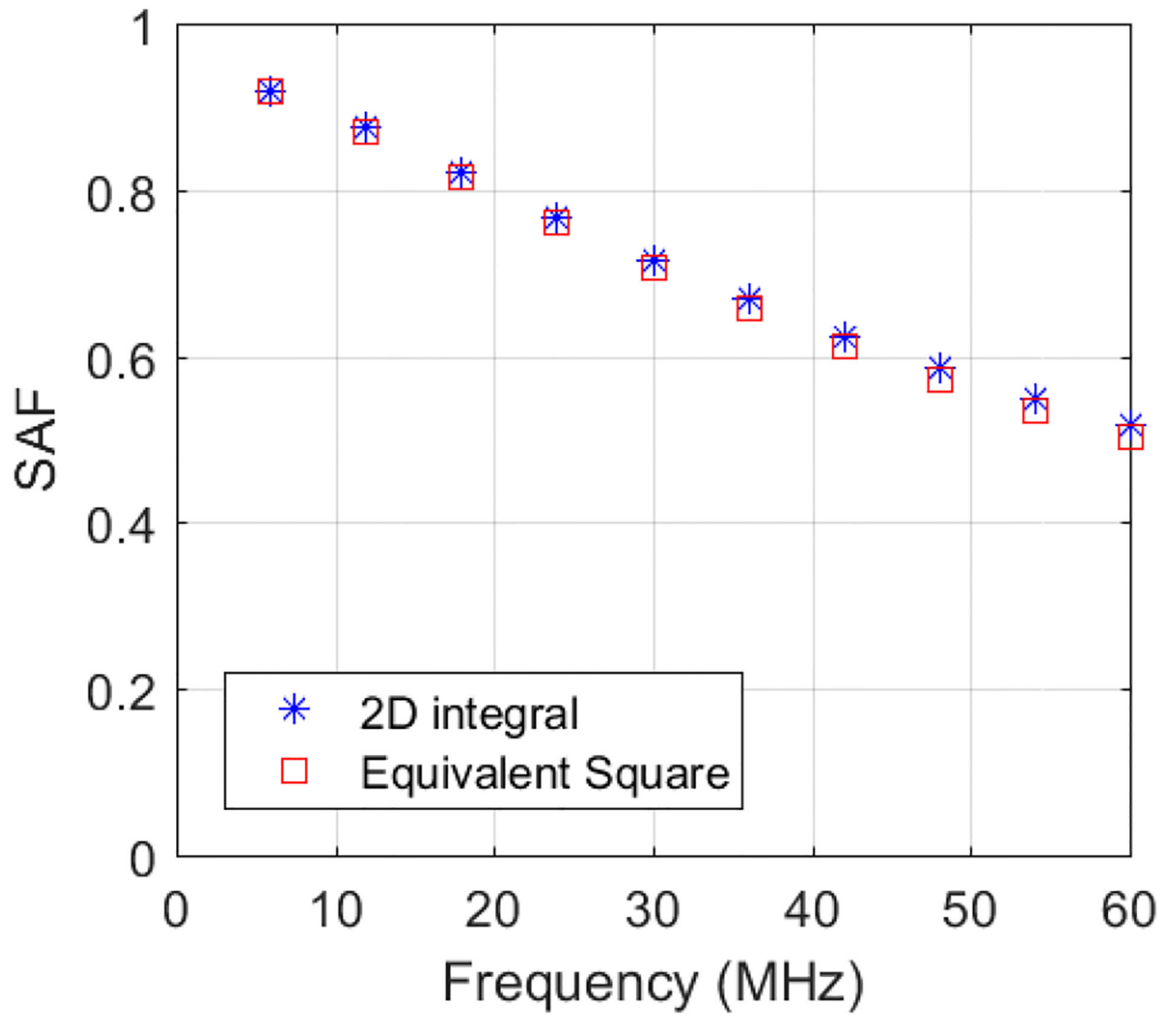
Fig. 4.
SAF, $S_p(nf_1)$, for the transducer in Fig. 3 and $d_g = 200~\mu$m. The 2-D integral is (10). The equivalent square hydrophone approximation is (15).
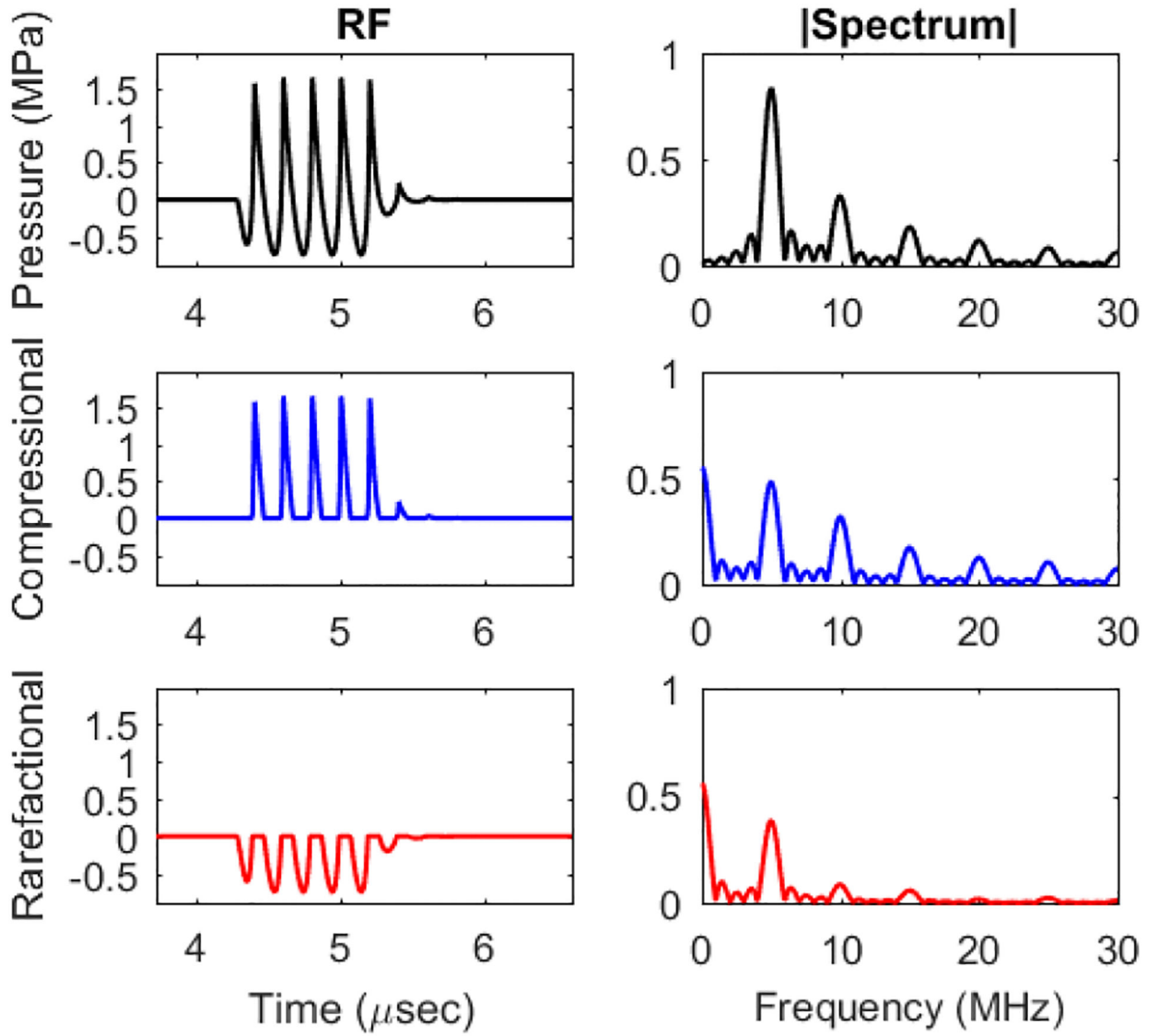
Fig. 5.
Tone burst decomposed into compressional and rarefactional components (left column).
Spectra show that most harmonic content is contained in the compressional component
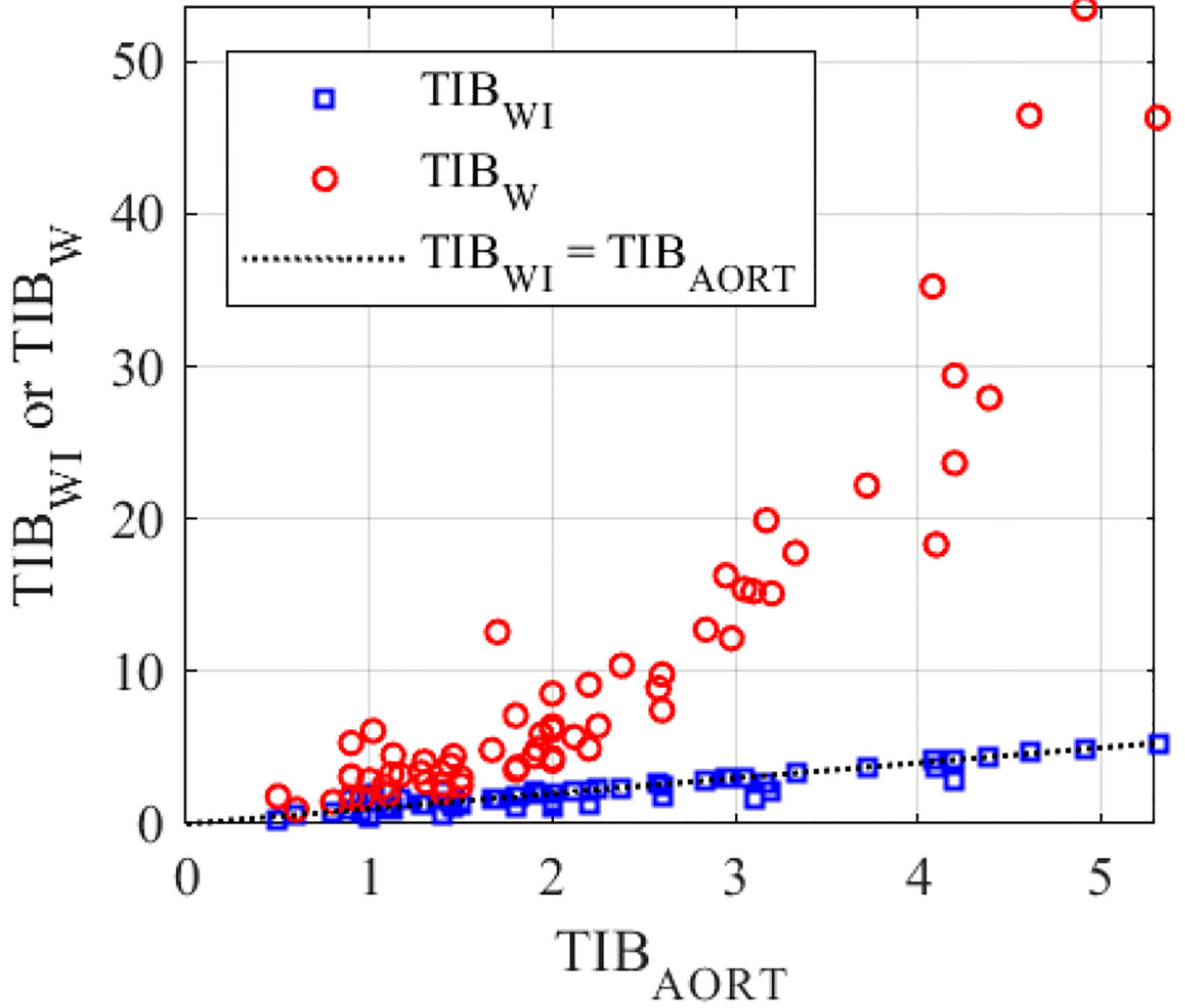(right column).

Fig. 6.
TIB_{WI} and TIB_W plotted versus the value of TIB given in the AORT, TIB_{AORT}, for pulsed Doppler signals. TIB is the minimum of TIB_{WI} and TIB_W, which was always TIB_{WI} for this data. See (20). These values are not corrected for hydrophone spatial averaging.
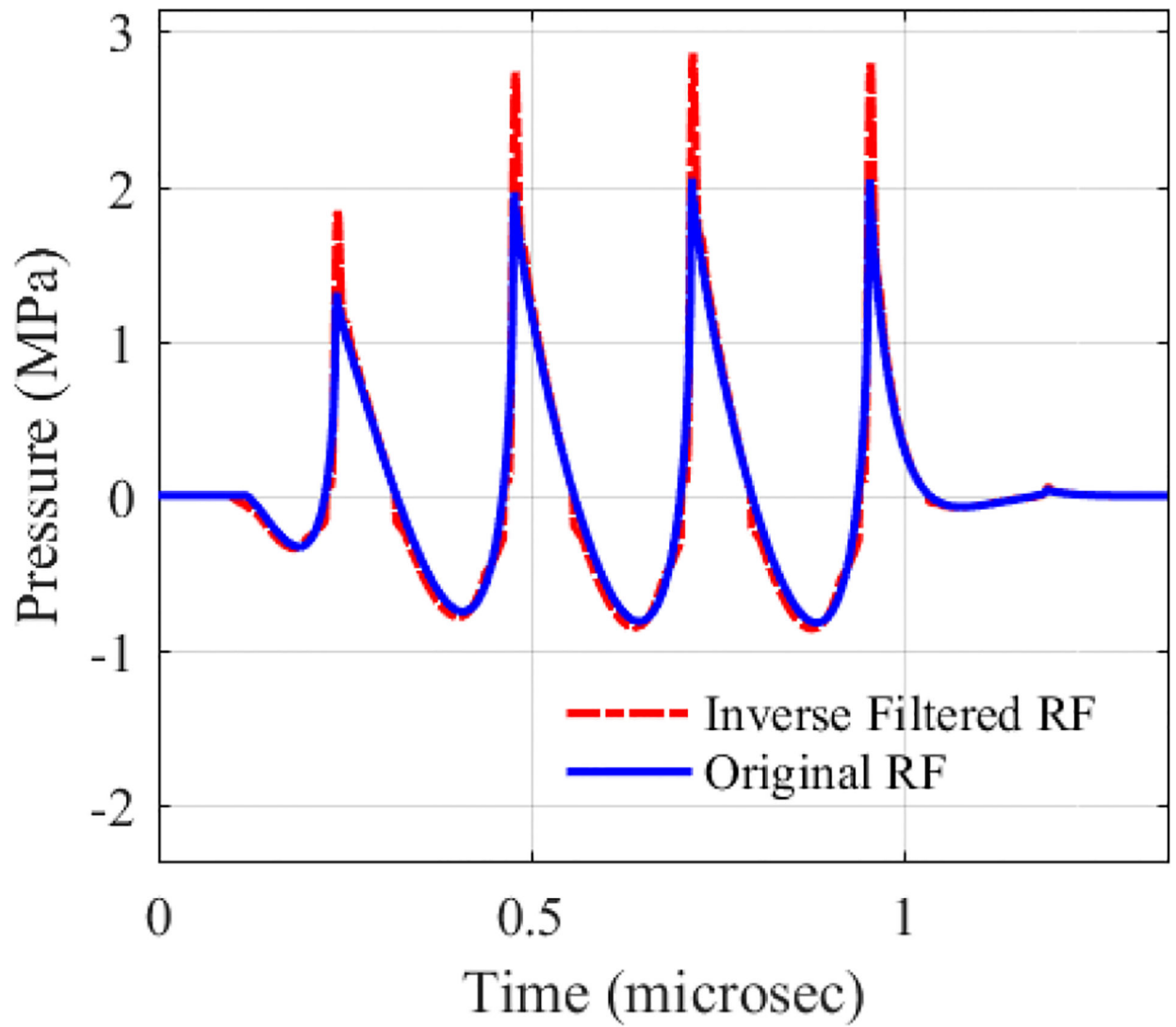
Fig. 7.
Simulated Doppler pulse before and after inverse filtering to correct for spatial averaging
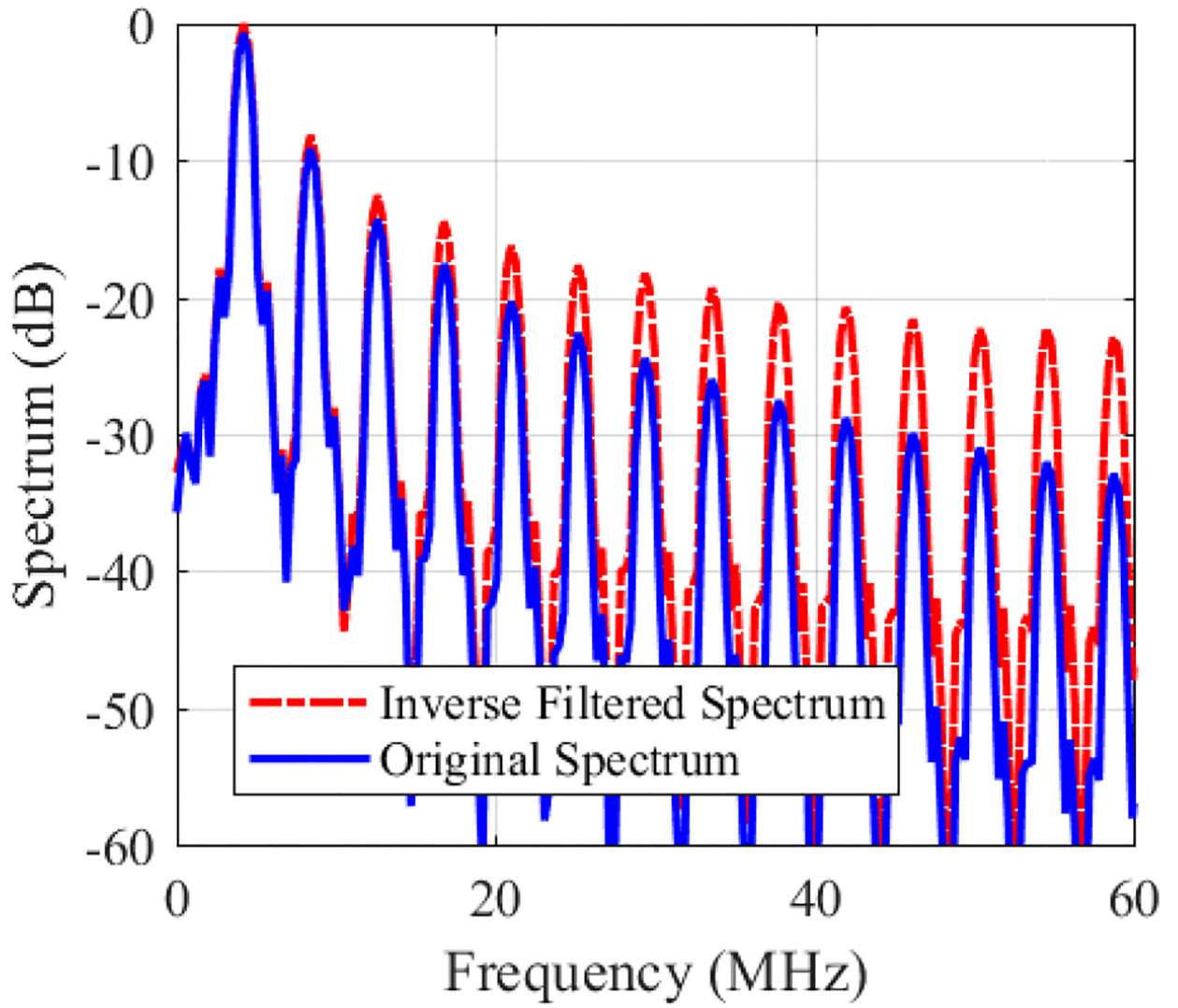effects.

Fig. 8.
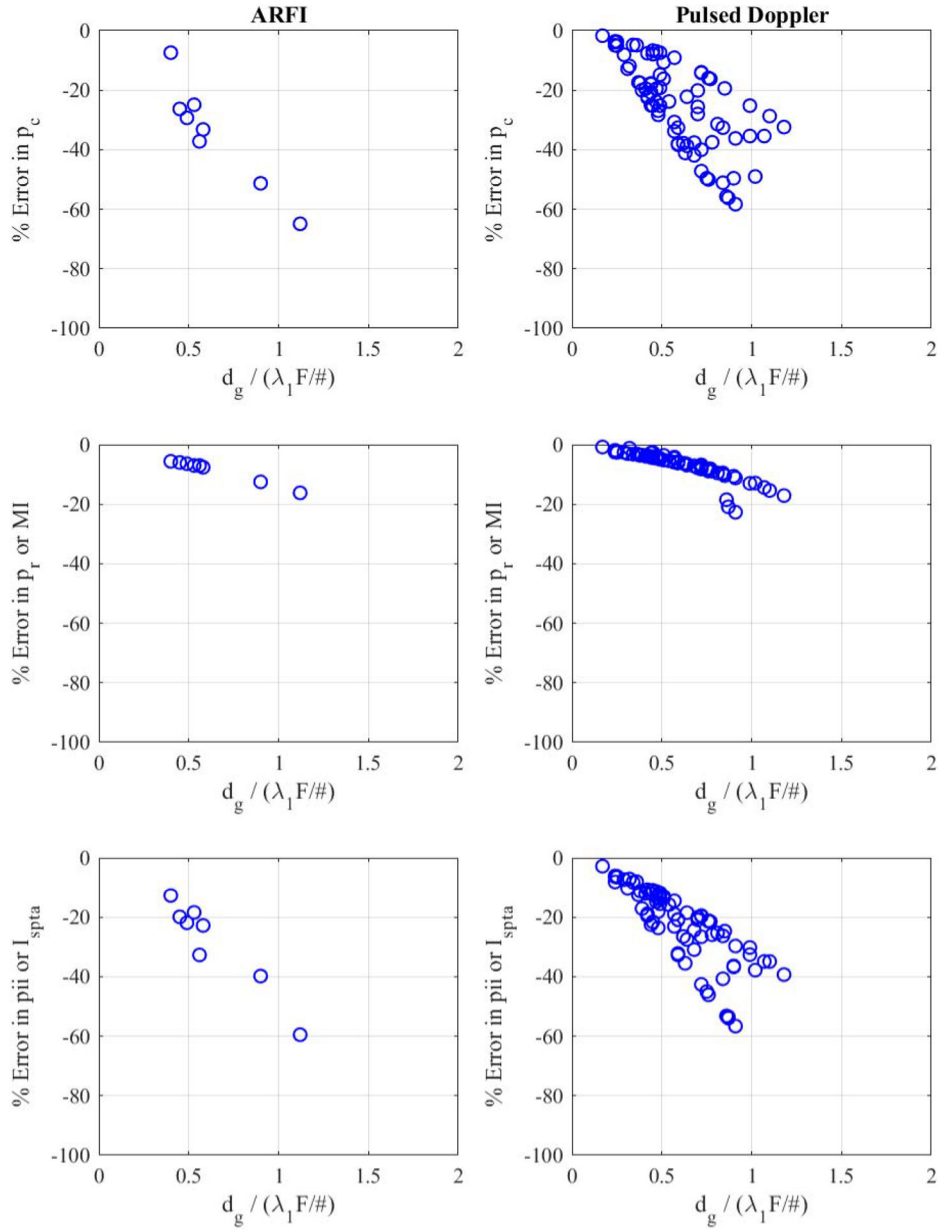Simulated spectra before and after inverse-spatial-averaging filtering.

Fig. 9.
Predictions of errors in p_c, p_r, pii, MI, and I_{spta} for simulated ARFI (left column) and Doppler (right column) pulses. The abscissa is the ratio of the hydrophone geometrical sensitive element diameter to the product of the fundamental wavelength λ_1 and the $F/\#$ (ratio of focal length to array width). The product $\lambda_1 F/\#$ is an index of the fundamental focal spot width because $FWHM_{1x} \approx 1.2\lambda_1 F/\#$ (see Section II-A).
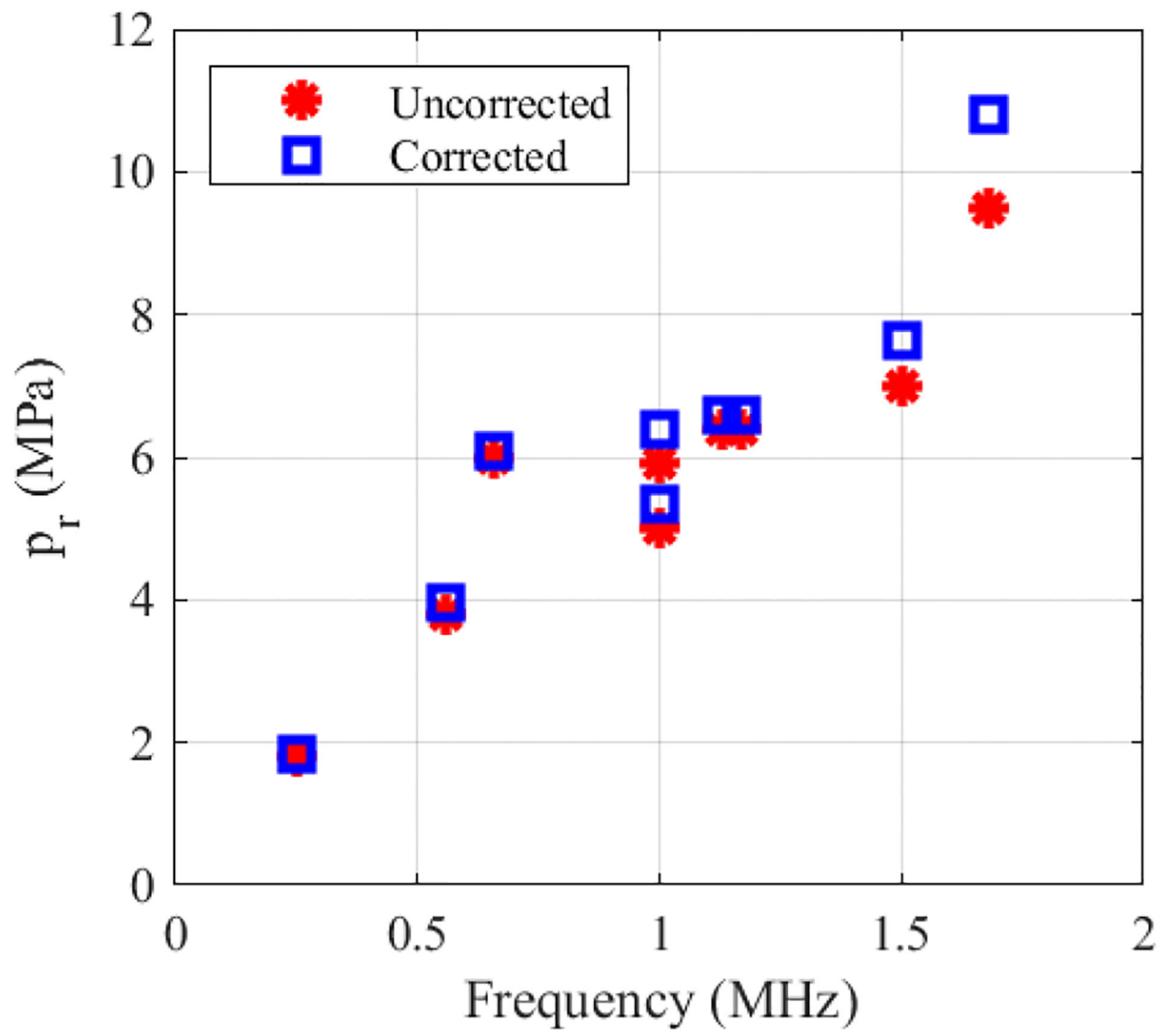
Fig. 10.
Cavitation thresholds from animal experiments in the literature uncorrected and corrected
for hydrophone spatial averaging. See Section V-D for details.

TABLE I

Acoustic Working Frequencies and Exposure Indexes

Parameter	ARFI	Pulsed Doppler
Frequency f_1 (MHz)	3.2 ± 1.3	4.1 ± 1.4
MI	1.6 ± 0.2	1.3 ± 0.3
TIS	1.1 ± 0.6	1.0 ± 0.5
TIB	1.6 ± 0.5	2.0 ± 1.0

All entries are means ± standard deviations.

TABLE II

Percent Difference Between Corrected and Uncorrected Values

Parameter	ARFI		Pulsed Doppler	
	Mean ± std. dev.	Range	Mean ± std. dev.	Range
p_c	60 ± 50	8 – 185	41 ± 34	2 – 140
p_r or MI	9 ± 4	6 – 19	7 ± 5	1 – 29
pii or I_{spta}	43 ± 39	15 – 147	33 ± 27	3 – 130
TIB	19 ± 15	7 – 57	15 ± 11	1 – 52
t_{43}	50 ± 41	16 – 158	42 ±31	5 – 142

std. dev.: standard deviation

TABLE III

Maximum Exposure Durations Recommended by Aium

TI	Obstetric, Neonatal Transcranial, Neonatal Spinal	Other except eye
> 6.0	0	0
5.0 – 6.0	0	< 15 s
4.0 – 5.0	0	< 1 min
3.0 – 4.0	0	< 4 min
2.5 – 3.0	< 1 min	< 15 min
2.0 – 2.5	< 4 min	< 1 hour
1.5 – 2.0	< 15 min	< 2 hours
1.0 – 1.5	< 30 min	No limit
0.7 – 1.0	< 60 min	No limit
< 0.7	No limit	No limit

The first category (Obstetric …) includes gynecologic when pregnancy is possible. The Other category includes adult transcranial, general abdominal, peripheral vascular, neonatal (except head and spine) and other scanning examinations except the eye. For obstetric examinations, monitoring of TIS is recommended through the first 10 wk from last menstrual period and TIB thereafter.